



Probing the activity origin of the enhanced methanol electrooxidation on Ni-induced PdNi_x(OH)_y-TaN/C catalyst with nitrogen vacancies

Na Ye^{a,1}, Pengcheng Zhao^{b,1}, Xiaoying Qi^a, Riguan Zhang^c, Binhang Yan^d, Wenchao Sheng^b, Zhao Jiang^{a,*}, Tao Fang^a

^a Department of Chemical Engineering, Shaanxi Key Laboratory of Energy Chemical Process Intensification, Engineering Research Center of New Energy System Engineering and Equipment, Xi'an Jiaotong University, Xi'an 710049, China

^b College of Environmental Science and Engineering, Tongji University, 1239 Siping Road, Shanghai 200092, China

^c State Key Laboratory of Clean and Efficient Coal Utilization, Taiyuan University of Technology, Taiyuan 030000, China

^d Department of Chemical Engineering, Tsinghua University, Beijing 100084, China

ARTICLE INFO

Keywords:

PdNi-TaN/C

Methanol oxidation reaction

In situ ATR-SEIRAS

DFT

Nitrogen vacancies

ABSTRACT

Engineering high-performance inexpensive TaN-modified Pd-based nanostructures for alkaline methanol oxidation reaction (MOR) has attracted extensive attention, yet the related enhancement mechanism of TaN for MOR remains lacked. The core-shell like Pd₃Ni₁-TaN/C catalyst decorated with Ni(OH)₂/NiOOH that contains highly dispersed Ni sites and nitrogen defects has been fabricated for the first time. The unsaturated coordination environment and core-shell like morphology of Pd₃Ni₁-TaN/C bring fruitful active sites and a down-shifted d-band center, making it a highly-efficient electrocatalyst for alkaline MOR (17.3-fold that of commercial Pd/C). Besides the electronic effects and surface defect sites of Pd₃Ni₁-TaN/C, TaN also helps MOR proceed via HCOO_{ad} pathway (non-CO) accompanied by enhanced OH adsorption induced by the addition of Ni. DFT (Density Functional Theory) calculations also further confirm the energy barrier of the formation of HCOO_{ad} intermediate and desorption energy of CO on Pd₃Ni₁-TaN/C are reduced. The introduction of Ni species and nitrogen vacancies enhances the CO tolerance evidently.

1. Introduction

To address the increasing energy and environment issues, the development of renewable and sustainable energy storage/conversion technologies has become an urgent mission [1,2]. Electrochemical energy conversion devices have been recognized as promising approaches to solve these challenges, such as fuel cells, electrochemical water splitting devices and metal-air batteries [1–8]. Recently, researchers have put eyes on direct alcohol fuel cells, such as methanol and ethanol, due to the properties of low cost, high specific energy and mild operating temperature [9–11]. During this process, the methanol oxidation reaction (MOR), as the anode half reaction of direct methanol fuels cells, is limited by sluggish kinetics because of the multiple-electrons transfer process [12]. Nowadays, precious metals like palladium (Pd) catalysts have shown enhanced reaction kinetics in alkaline media [12]. Unfortunately, the high price, low abundance, and poor durability restrict its commercialization [1]. Therefore, it is urgent to explore

high-performance and inexpensive Pd-based catalysts for the large-scale application of efficient energy devices.

As the Sabatier principle said, the variation of the electronic structure can modulate the adsorption energy of intermediates, thus the catalytic performance is closely associated with the electronic structure of the electrocatalyst [3]. The incorporation of a second metal into Pd-based catalysts has been proved as an efficient approach to improve the catalytic activity by means of the electronic structure tuning [13]. In particular, Wu et al. [13] highlighted that the crucial roles of the second metal nanocrystals with oxophilic properties in the enhanced alcohol electrooxidation reactions through tuning the adsorption energy of hydroxyl species (OH_{ad}). Experimentally, our previous study [14] also clarified the importance of OH_{ad} species for alkaline MOR by in situ attenuated total reflection-surface enhanced infrared absorption spectroscopy (ATR-SEIRAS) spectroscopy, namely the bifunctional mechanism. Recently, transition metal nitrides (TMNs) have been regarded as extremely promising nanomaterials because of the multiple advantages

* Corresponding author.

E-mail address: jiangzhao@mail.xjtu.edu.cn (Z. Jiang).

¹ These authors contributed equally to this work and should be regarded as co-first authors.

of TMNs, such as low cost, rich resource and Pt-like electronic property [15–18]. Through facile heteroatom doping, the strong charge transfer between metal compounds and TMNs can modulate their electronic structures, resulting in an increase in active sites and enhancement in catalytic performance [16,19]. He et al. [15] reported the combination of Ta_3N_5 and $\text{Co}(\text{OH})_2$ significantly enhanced the solar water oxidation performance via generating a Ta-O-Co interface between them. Xiao et al. [17] synthesized a novel photocatalyst by the combination of Mg, Pt/ CoO_x and Ta_3N_5 , which showed the effectively improved activity of solar hydrogen production. However, to date, most of the applications of TMNs are photocatalysts, the related reports on the application in electrocatalysts of TMNs are extremely lacked, especially for TaN [18]. And almost all the fundamental surface science researches are dominated by the former. Meanwhile, TMNs-decorated Pd-based electrocatalysts with modulated electronic configuration and Pt-like electronic properties are expected to be promising electrocatalysts, and are also of great economic interest and scientific significance. Therefore, it is also urgent to develop the application of TMNs in electrocatalysts. In our previous report [20], the construction of the PdCu-TaN interface enhanced the CO tolerance ability and the electrocatalytic performance for the alkaline MOR. Nevertheless, the inherent structural characteristics of TaN and performance enhancement mechanisms of the alkaline MOR at the atomic level on the TaN-doped Pd-based electrocatalysts are still unclear. Taken together, it is expected that the combination of more oxophilic second metals and TMNs into Pd catalysts will be highly likely to achieve a further elevated electrocatalytic MOR performance by modulating the intrinsic electron configuration. Meanwhile, understanding the respective roles of TMNs and the oxophilic metals may shed light on the rational design of the novel and cheap TMNs-doped Pd-based electrocatalysts with high efficiency for alkaline direct alcohol fuel cells.

On the base of the above analysis, considering that Ni presents more oxophilic features than Cu, this work focuses on the fabrication of highly-efficient TaN-modified Pd-Ni nanostructures for alkaline MOR and clearly elucidating of the roles played by TaN and oxophilic second metal. Additionally, the specific structure-performance relationships and reaction pathway at the atomic level are also required to be clarified. In the work, $\text{Ni}(\text{OH})_2/\text{NiOOH}$ decorated $\text{Pd}_3\text{Ni}_1\text{-TaN/C}$ catalyst with modulated electron configuration as well as surface defects has been constructed by a mild solvothermal approach for the first time, whose structure is determined by a series of characterization techniques. Owing to the unique structure, $\text{Pd}_3\text{Ni}_1\text{-TaN/C}$ catalyst presents the markedly elevated catalytic activity, durability and anti-CO poisoning ability towards MOR in alkaline media, making it promising to be an efficient anode catalysts for direct methanol fuel cells. Then, a combination of the *in situ* ATR-SEIRAS technique and DFT calculations is used to identify the reaction intermediates and further elucidate the reaction mechanism, which is also the first fundamental surface science research on the alkaline MOR over $\text{Pd}_3\text{Ni}_1\text{-TaN/C}$ catalyst. The work provides a facile strategy to the construction of TaN-modified Pd-based nanostructures and also offers a new and comprehensive methanol electro-oxidation enhancement mechanism on TaN-modified Pd-based nanostructures at the molecular level.

2. Experimental

2.1. Chemicals and materials

Sodium tetrachloropalladate (Na_2PdCl_4 , 99.9%), nickel chloride hexahydrate ($\text{NiCl}_2 \cdot 0.6 \text{H}_2\text{O}$, 99.9%) and Tantalum nitride (TaN, 99.5%) were obtained from Aladdin. Potassium hydroxide pellets (KOH, 85%) were bought from Sigma Aldrich. Cetyltrimethyl ammonium bromide (CTAB, 99.0%), ethylene glycol (EG, AR), ethanol (AR) and methanol (AR) were obtained from Sinopharm Chemical Reagent limited corporation. Cabot carbon black (VXC-72R) was obtained from Kingchemical company. Argon and carbon monoxide (20%) gas were obtained from

Xi'an Tianze gas company. Ultra-pure water ($18.2 \text{ M}\Omega\text{-cm}$) was used for all the electrochemical tests. All chemicals were analytical grade reagents and used without further purification.

2.2. Synthesis of $\text{Pd}_3\text{Ni}_1\text{-TaN/C}$, Pd/TaN-C and $\text{Pd}_3\text{Ni}_1\text{/C}$ catalysts

$\text{Pd}_3\text{Ni}_1\text{-TaN/C}$ catalysts were synthesized as follows: First, TaN (270 mg), VXC-72 Cabot black (135 g) and CTAB (500 mg) were added into EG (67.5 mL). Then, the solutions was stirred and sonicated for 1 h to mix uniformly. After that, Na_2PdCl_4 solution ($19 \text{ g}\cdot\text{L}^{-1}$), $\text{NiCl}_2 \cdot 0.6 \text{H}_2\text{O}$ ($10 \text{ g}\cdot\text{L}^{-1}$) and KOH aqueous solution were added to the above mixture, and heated at 120°C for 2 h. After the reaction, the reactor was naturally cooled down to room temperature, and the products were washed by centrifugation with ethanol and water three times. Finally, the $\text{Pd}_3\text{Ni}_1\text{-TaN/C}$ catalysts were obtained after the vacuum drying at 343 K for 24 h. ICP-MS was conducted to determine the actual loadings of Pd (3.2 wt %) and Ni (0.52 wt %), proving that the Pd and Ni precursors had been effectively reduced (Table S1). In comparison, the Pd-TaN/C catalyst was synthesized by the similar method above except the absence of Ni precursors. And the $\text{Pd}_3\text{Ni}_1\text{/C}$ catalyst was obtained by the similar method above except the absence of TaN.

2.3. Catalyst characterization

To study the crystal structures, X-ray diffraction (XRD) patterns were obtained at the BL14B1 beamline of the Shanghai Synchrotron Radiation Facility (SSRF) using a 0.06887 nm wavelength X-ray. Meanwhile, XRD patterns were also obtained by XRD (Bruker D8 Advance) with Cu $K\alpha$ radiation (operated at 40 kV and 40 mA, $\lambda = 1.5406 \text{ \AA}$), as shown in supporting information. The morphologies and average particles sizes were evaluated using a highly annular dark-field (ADF) imaging in an aberration-corrected scanning transmission electron microscope (STEM, JEM-ARM300F (GrandARM)). To study the surface compositions and chemical states, X-ray photoelectron (XPS) spectra (XPS, Thermo Fisher ESCALAB Xi⁺) were acquired on a spectrometer with a Al- $K\alpha$ radiation (1486.6 eV). The inductively coupled plasma-mass spectroscopy (ICP-MS, NexION 350D) was used to determine the actual loadings of catalysts. To further study the local coordination environments and valence states, synchrotron-based X-ray absorption fine structure (XAFS) experiments of Ni K-edge and Ta L3-edge were carried out at the 4B9A beamline of the Beijing Synchrotron Radiation Facility (BSRF).

2.4. *In situ* ATR-SEIRAS measurements

In situ attenuated total reflection-surface enhanced infrared absorption spectroscopy (ATR-SEIRAS) was used to identify the reaction intermediates and further elucidate the MOR reaction mechanism. Detailed procedures were according to the reported studies and displayed in Supporting Information (SI).

2.5. Electrochemical tests

All the electrochemical experiments were conducted with a electrochemistry workstation (CHI 650B) in a three-electrode cell, consisting of Pt wire (counter electrode) and silver/silver chloride electrode (reference electrode). Electrocatalysts (4 mg) and 5 wt% Nafion solution (Dupont, 40 μL) were dissolved into 1 mL of aqueous isopropanol (20% isopropanol) and mixed ultrasonically to achieve good homogeneous dispersion. Finally, 10 μL of the suspension was cast onto the surface of the glass carbon electrode (GC, 5 mm diameter), which was used as the working electrode. For all the electrochemical tests, the solutions need to be bubbled with an inert gas such as Ar to be deoxygenated before the measurements. Besides, to remove the contaminants on the surface, the catalysts need to be activated by potential scanning from 0 to 1.4 V (vs RHE) in a 0.5 M H_2SO_4 or 1 M KOH solution till obtaining a stable cyclic voltammograms (CV) curve. Then MOR CV test was conducted in the

presence of methanol at a scan rate of 50 mV s⁻¹ for 20 scans in the range of 0–1.4 V vs. RHE, where the 20th scan was applied in this work.

2.6. DFT calculations

DFT calculations were performed employing the Vienna Ab-Initio Simulation Package (VASP) code [21]. The electronic exchange and related effects were treated by the generalized gradient approximation with the Perdew, Burke and Ernzerhof (PBE) functional [22]. The kinetic wave cutoff energy was set to be 400 eV to depict the electronic wave functions. The Brillouin-zone integration was sampled using a $3 \times 3 \times 1$ Monkhorst-Pack k-points grid along with a Gaussian smearing of 0.1 eV [23]. The energy convergence criterion of 1×10^{-5} eV was applied. The Pd(111) surface was modeled by a four-layer 3×3 super-cell covered with 1/9 monolayer of the selected adsorbates. TaN(001) and Pd/TaN(001) and PdNi/TaN(001) was modeled by a 2×2 super-cell with three layers. Regarding the Pd/TaN(001) and PdNi/TaN(001) surface, Pd₄ and Pd₄Ni(OH)₂ clusters were deposited on the TaN(001) surface, which was applied to be the most stable configurations as the interfacial models for Pd/TaN as well as PdNi/TaN. Regarding the Pd₄Ni(OH)₂-TaN(001)-V surfaces, Pd₄ and Pd₄Ni(OH)₂ clusters were deposited on the TaN(001) surface with nitrogen vacancies. The above models are displayed in Fig. S1 (Supporting Information). The bottom layers were fixed, and other layers can be relaxed. We add a 20 Å vacuum layer perpendicular to the slab to avoid artificial interactions between the slab and its periodic images. The transition state structure of the reactions is located by employing the nudged elastic combined with minimum-mode following dimer method. All the transition states were determined by vibration analysis.

The binding energies (BE) for all adsorbed intermediates are defined as follows:

$$BE = E_{\text{adsorbate/surface}} - E_{\text{adsorbate}} - E_{\text{surface}} \quad (1)$$

where $E_{\text{adsorbate/surface}}$ is the total energy between the adsorbate and the surface, $E_{\text{adsorbate}}$ is the total energy of the free adsorbate in the gaseous phase, and E_{surface} is the total energy of the surface.

3. Results and discussion

3.1. Characterization of the Pd₃Ni₁-TaN/C and Pd-TaN/C catalysts

The PdNi-TaN and Pd-TaN supported on carbon catalysts are constructed by a mild one-pot ethylene glycol method. The crystalline structures of the Pd₃Ni₁-TaN/C, Pd-TaN/C and the reference catalysts (Pd₃Ni₁/C and commercial Pd/C) are investigated by XRD analysis, as shown in Fig. 1 and Fig. S2. The intense diffraction peaks marked by * in the XRD patterns of the Pd₃Ni₁-TaN/C and Pd-TaN/C catalysts are assigned to the planes of TaN (JCPDS Card No. 39–1485). Other small peaks (marked by Δ, ∇, °, □) in Fig. 1 can be assigned to tantalum (oxy) nitride. Meanwhile, it can be found that these patterns above match well with those of the pristine TaN/C in Fig. S2 and that no detectable peaks of Pd or Ni/NiO_x species are observed, which may be attributed to the strong diffraction intensity of TaN and low loadings of Pd/Ni [24,25]. This also indicates that the addition of Ni may not bring the variation in the crystalline structure of Pd₃Ni₁-TaN/C.

Subsequently, the morphologies and average particles sizes of Pd₃Ni₁-TaN/C are characterized by TEM, HRTEM and HAADF-STEM (atomic-scale high angle annular dark-field scanning TEM) images in Fig. 2 and Fig. S3. Obviously, the monodispersed PdNi nanoparticles with spherical-like shapes supported on carbon are observed in TEM images (Fig. S3(a, b)), revealing that the nanoparticles exhibit good dispersity without evident aggregation. As seen in TEM images of Fig. 2(a), the average nanoparticle sizes of Pd₃Ni₁-TaN/C is about 2.58 nm by the statistical method. Furthermore, in HAADF-STEM images of Fig. 2(b, c) and Fig. S3(c, d), the measured lattice spacing of 0.22 nm and

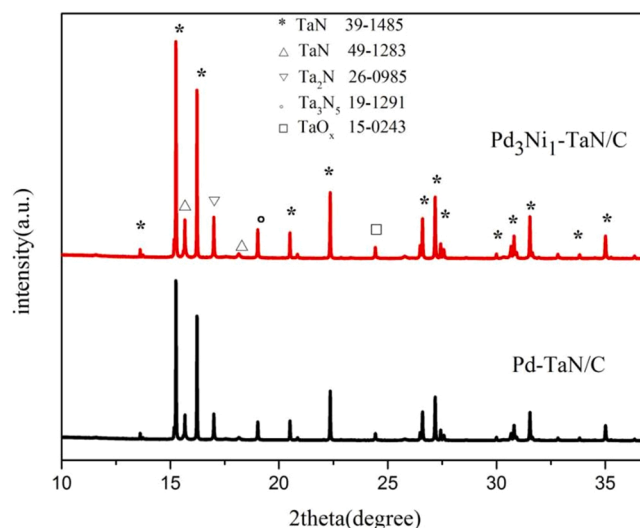


Fig. 1. XRD patterns of Pd₃Ni₁-TaN/C and Pd-TaN/C catalysts.

0.15 nm correspond to the Pd(111) and TaN(300) planes of the Pd₃Ni₁-TaN/C catalyst, indicating the presence of highly crystalline Pd and TaN.

Besides, the EDX element mappings are performed as shown in Fig. 2(d-k) and Fig. S3(e-m). Interestingly, the Ta element is preferentially distributed in the outer layer (shell region) of the C element (core region) to form a core/shell-like structure (Fig. 2f), similar to the previous report [26]. The N element is uniformly dispersed the whole shell and core regions. This results indicate that TaN/C prefers to form a special core/shell-like structure by the solvent thermal reduction method, which may provide the surface space for the Pd and Ni active compositions. As shown in Fig. 2(d-k), it can be also found that the Pd and Ni elements are highly dispersed on the TaN/C surface. However, from the overlay mappings, it is indicated that the Pd and Ni elements are distributed unevenly, in which the Ni element prefers to being atomically dispersed on the TaN-C surface and Pd element is favorable to form around 2.6 nm particles, suggesting that Pd and Ni may be not alloyed perfectly.

Furthermore, the surface composition and chemical states are studied through XPS survey in Fig. 3, Fig. S4 and Table S2, in which all peaks are calibrated by locating the C 1s peak at 284.8 eV. The high-resolution Pd 3d spectrum of the Pd₃Ni₁-TaN/C catalyst is shown in Fig. 3(a). It is observed that the relative percentages of Pd⁰ in the Pd₃Ni₁-TaN/C, Pd-TaN/C and Pd₃Ni₁/C catalysts are 83.9 %, 77.2 % and 83.6 %, respectively, suggesting that the metallic Pd is the main form for all the catalysts (Table S2). Moreover, it is also found that, compared to the Pd₃Ni₁/C catalyst, the binding energy of Pd 3d peak of Pd₃Ni₁-TaN/C exhibits a negative shift of 0.1 eV, indicating that the introduction of TaN will bring Pd into the electron-rich state. However, relative to Pd/TaN-C, a positive shift by 0.1 eV is observed for the Pd 3d peak of Pd₃Ni₁-TaN/C, suggesting that the doped-Ni inhibits the electron transfer to Pd. Therefore, we can propose that the existence of TaN and Ni bring charge transfer among the Pd₃Ni₁-TaN/C catalyst. The possible transfer mechanism may be that TaN transfers electrons to Pd, while Pd transfers electrons Ni on the surface of Pd₃Ni₁-TaN/C catalyst [27,28]. This indicates the chemical structure of Pd₃Ni₁-TaN/C is altered after the incorporation of Ni, and is also evidence of the interaction between PdNi and TaN.

The high-resolution Ni 2p_{3/2} spectrum of the Pd₃Ni₁-TaN/C catalysts in Fig. 3(b) can be fitted with four peaks, including Ni, NiO, Ni(OH)₂ and NiOOH [29–31], whose relative contents are 2.22 %, 9.02 %, 58.06 % and 30.71 %, respectively. The results indicate that high-valence Ni^{δ+}, oxides or hydroxides, plays a major role on the Pd₃Ni₁-TaN/C surface, which might be attributed to the alkaline synthesis method and easily oxidized properties of Ni [32]. Furthermore, the high-resolution Ta 4f spectrum

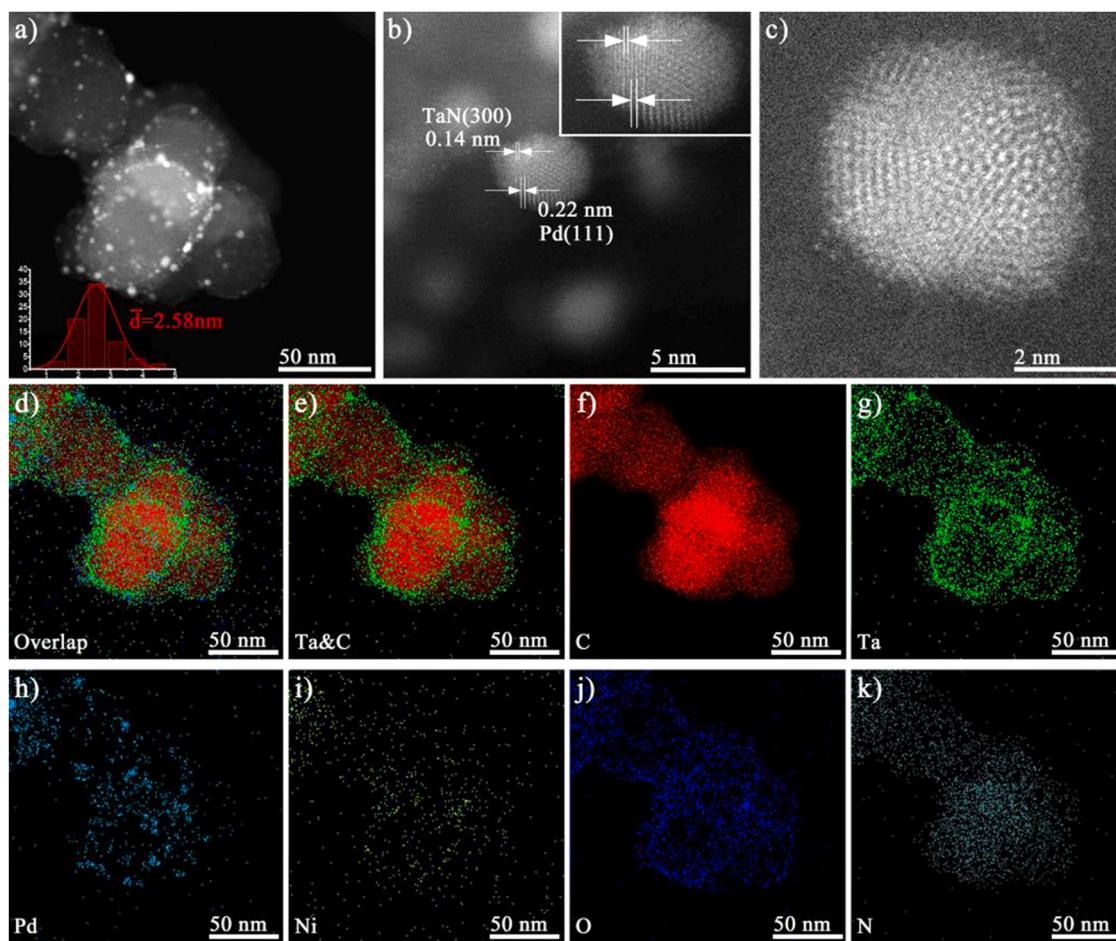


Fig. 2. Low magnification (a) and high magnification (b, c) HAADF-STEM images of the Pd₃Ni₁-TaN/C catalyst. The corresponding STEM-EDS elemental mapping (d–k) of the Pd₃Ni₁-TaN/C catalyst.

of the Pd₃Ni₁-TaN/C catalysts in Fig. 3(c) can be fitted with three parts, corresponding to: N-Ta-N (tantalum nitride), N-Ta-O (tantalum (oxy) nitride) and O-Ta-O (tantalum oxide) [33–36]. The results are in agreement with above XRD analysis. It is found that the contents of N-Ta-N, N-Ta-O and O-Ta-O in the Pd₃Ni₁-TaN/C catalyst are 7.8%, 80.1% and 12.1%, respectively. On the Pd-TaN/C catalyst surface, the content of N-Ta-N, N-Ta-O and O-Ta-O are 10.3%, 78.0% and 11.7%, respectively. It can be found that N-Ta-O bond is the main peak for both Pd₃Ni₁-TaN/C and Pd-TaN/C catalysts. However, the tantalum (oxy) nitride is hardly observed in XRD patterns. Thus, it may be assumed that tantalum (oxy)nitrides in Pd₃Ni₁-TaN/C catalysts are likely present in the amorphous state. Moreover, compared to the Pd-TaN/C, it is found that a negative shift of the N-Ta-O bond in Pd₃Ni₁-TaN/C is 0.2 eV. It might result from the promoting incorporation of Pd into the N-Ta-O bond in the presence of Ni since Pd exhibits higher electronegativity than Ta, which is similar to previous reports [24] and confirmed by above EDX element mappings analysis. Taken together, the above XPS analysis confirms the unique electronic configuration, that is, strong electronic interactions between PdNi and TaN.

For the purpose of further making sense the presented chemical state of Ni and the effect of Ni incorporation on the electronic structure of Pd₃Ni₁-TaN/C, synchrotron-based X-ray absorption fine structure (XAFS) technique is employed to track the local coordination environments and valence states of Pd₃Ni₁-TaN/C and Pd-TaN/C. X-ray absorption near-edge structure (XANES) spectra are performed to uncover the oxidation states of Ni. The normalized Ni K-edge XANES spectra of the catalysts are shown in Fig. 4(a), in which Ni foil, NiO, Ni(OH)₂ and NiOOH are selected as the reference materials. For Ni K-edge XANES

features, the absorption edge energy is determined by an integral strategy, the position of which can be directly related to the variation of Ni oxidation states [37–44], as shown in Fig. S5a. The average oxidation state of Ni cation in Pd₃Ni₁-TaN/C can be quantified to be +2.4 by a comparison of the edge energy positions to those of the reference materials (as shown in Fig. S5b) [40,45,46], indicating that the Ni species in Pd₃Ni₁-TaN/C is a mixture of Ni oxides, which is also consistent with the XPS results.

Extended X-ray absorption fine structure (EXAFS) results are employed to probe the short-range local coordination environment of the catalysts by revealing the distances between the absorbed metal atoms and scattered atoms [47]. Fig. 4(b) gives the Fourier transform (FT) EXAFS spectra at Ni K-edge in R space of the catalysts. It can be indicated that two peaks exist, where the peak at around 1.5 Å (without phase correction) represents Ni-O path, arising from the scattering from the absorbing metal atom (Ni) to its closest neighboring O, and the peak at around 2–3 Å (without phase correction) represents Ni-Ni (or Ni-O-Ni) path, arising from the scattering from the absorbed metal atom (Ni) to its closest neighboring Ni [37,48,49]. Fig. 4(c) presents a further spectral fitting of EXAFS in R space to provide quantitative information. As seen from Fig. 4(b) and Fig. 4(c), for NiO, the intensity of the peak at 2.95 Å representing the interatomic Ni-O-Ni distance is much higher than that at 2.08 Å representing the interatomic Ni-O distance. For Ni(OH)₂, the intensity of the peak at around 3.12 Å corresponding to the Ni-O-Ni distance is similar to that of Ni-O distance at 2.06 Å. However, for Pd₃Ni₁-TaN/C, the intensity of the Ni-O-Ni distance at 3.04 Å is much lower than that of Ni-O distance at 2.05 Å, which is similar to that for NiOOH. The results indicate that Pd₃Ni₁-TaN/C is preferentially

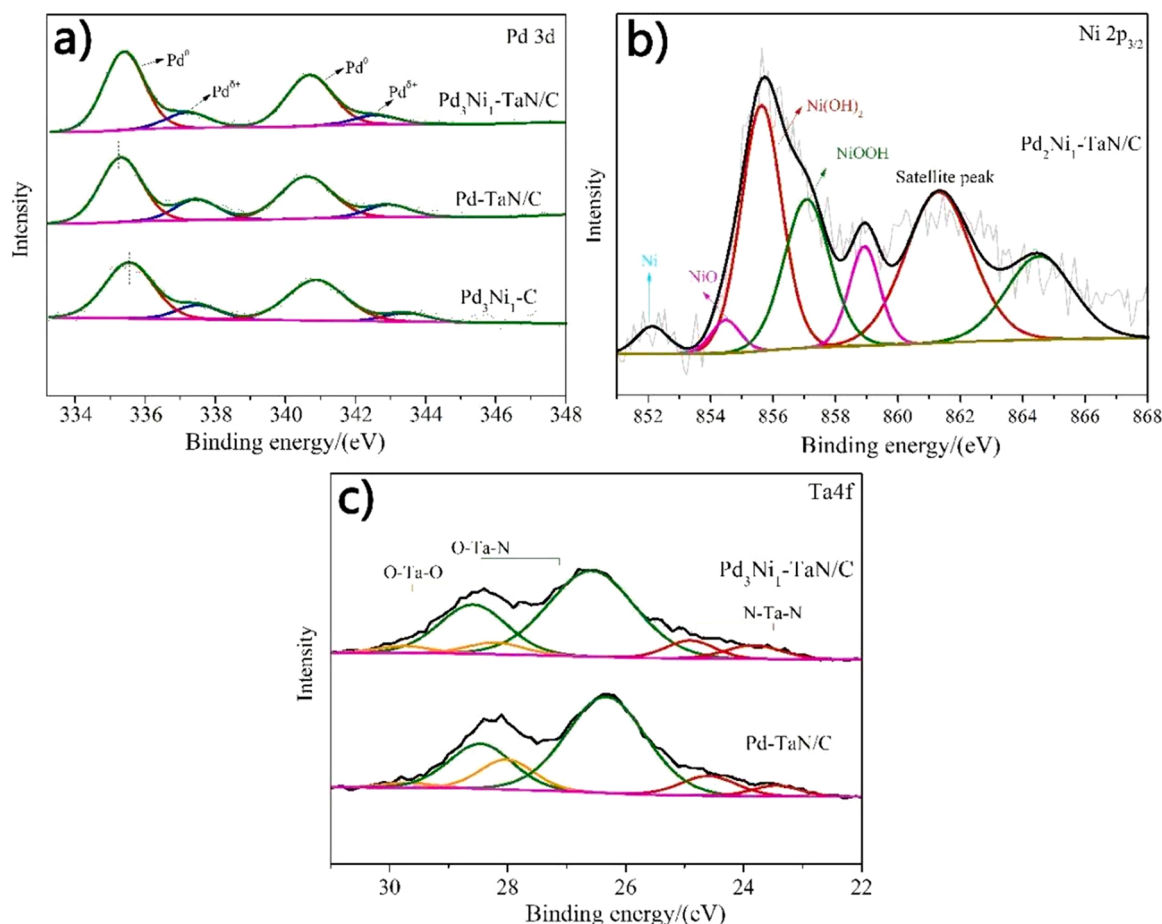


Fig. 3. High-resolution XPS spectra of Pd 3d (a), Ni 2p (b), and Ta 4f (c) for the Pd₃Ni₁-TaN/C, Pd₃Ni₁/C and Pd-TaN-C catalysts.

covered by the Ni-O (metal-O) distance rather than the Ni-Ni (metal-metal) distance, which may be due to that Ni atoms prefer to be coordinated with O atoms and atomically disperse on Pd₃Ni₁-TaN/C in the form of Ni_xO_y ultra-fine clusters, similar to the previous reports [50–54]. This is further evidenced by the fitted coordination number results of the catalysts.

Specifically, for Pd₃Ni₁-TaN/C, the fitting results of Ni-O path in Ni EXAFS spectra (Table 1, Table S3 and Fig. 4c) show that Ni in these catalysts (except Ni foil) is coordinated with six neighboring O atoms, identical with that for other referenced Ni oxides, suggesting that Ni is fully coordinated by O atoms at the first peak [55]. Meanwhile, the Ni EXAFS fitting results (as shown in Table 1, Table S3 and Fig. 4c) also indicate that the coordination number of Ni-Ni at the distance of 3.04 Å for Pd₃Ni₁-TaN/C is reduced to 3.1, much lower than the theoretical value of six for other referenced Ni oxides, indicative of a highly under-coordinated Ni-Ni path at the second peak [56,57]. Overall, the obviously weakened intensity as well as lower coordination number of Ni-Ni for Pd₃Ni₁-TaN/C relative to other Ni oxides suggest that it is likely that Pd₃Ni₁-TaN/C possesses more atomically dispersed feature of Ni or large amounts of small-size Ni oxides clusters, consistent with the HAADF-STEM results, which has also been displayed in similarly reported EXAFS studies [9, 51, 54, 58–61]. At the same time, the reduced ratio of the Ni-Ni and Ni-O paths is also an indicator of the generation of nickel defects (or nickel vacancies) [3,62,63]. Wavelet-transform (WT)-EXAFS analysis is also performed at the Ni K-edge for these catalysts, as shown in Fig. 5(a). Different from the strong signal of Ni-O-Ni path (or Ni-Ni path) for Ni(OH)₂, NiO and Ni foil, there exists a strong signal of Ni-O path for Pd₃Ni₁-TaN/C, which is in agreement with the EXAFS results. Meanwhile, for the Ni-O-Ni path, the WT maximum for

Pd₃Ni₁-TaN/C (5.0 Å⁻¹) presents a lower *k* value than that for Ni(OH)₂ (6.9 Å⁻¹), NiO (6.9 Å⁻¹) and Ni foil (7.3 Å⁻¹), indicating that the structural order of Ni-O-Ni for Pd₃Ni₁-TaN/C is lower relative to other Ni oxides and Ni foil [64]. Taken together, these results imply that the content of Ni-O-Ni in Pd₃Ni₁-TaN/C is low, that is, the proportion of Ni defects is higher [65]. In addition, as seen from the fitting results in Table 1, there are two main peaks for Pd₃Ni₁-TaN/C, one is the interatomic Ni-O distance at 2.05 Å close to that of Ni(OH)₂ and the other is the interatomic Ni-O-Ni distance at 3.04 Å close to the longer interatomic Ni-O-Ni distance at 3.05 Å of NiOOH. The results imply that Ni element is present in the form of a mixture containing Ni(OH)₂ and NiOOH in Pd₃Ni₁-TaN/C, in accordance with the Ni K-edge XANES results and XPS analysis.

Furthermore, to further figure out the effect of Ni incorporation on the chemical state and atomic structure of Pd₃Ni₁-TaN/C, XANES and EXAFS are carried out on both Pd₃Ni₁-TaN/C and Pd-TaN/C to track their local coordination environments and valence states. Fig. 4(d) displays the normalized Ta L3-edge XANES spectra of Pd₃Ni₁-TaN/C, Pd-TaN/C and their reference compounds. As can be seen from Fig. 4(d), for these reference compounds, a positive shift occurs in the Ta L3-edge features for Ta foil, TaN and Ta₂O₅ in the energy range between 9875 eV and 9882 eV, indicating that the Ta valence state gradually increases in Ta foil (as a reference metal), TaN (as reference nitrides) and Ta₂O₅ (as reference oxides) [66]. At the same time, it can be also found that both the energy positions of Pd-TaN/C and Pd₃Ni₁-TaN/C are very close to the TaN standard reference purchased from Aladdin, suggesting that they have a similar Ta valence states [39,56,67].

The comparison of the FT of *k*²-weighted Ta L3-edge EXAFS spectra for the catalysts is displayed in Fig. 4(e), where two main contributions

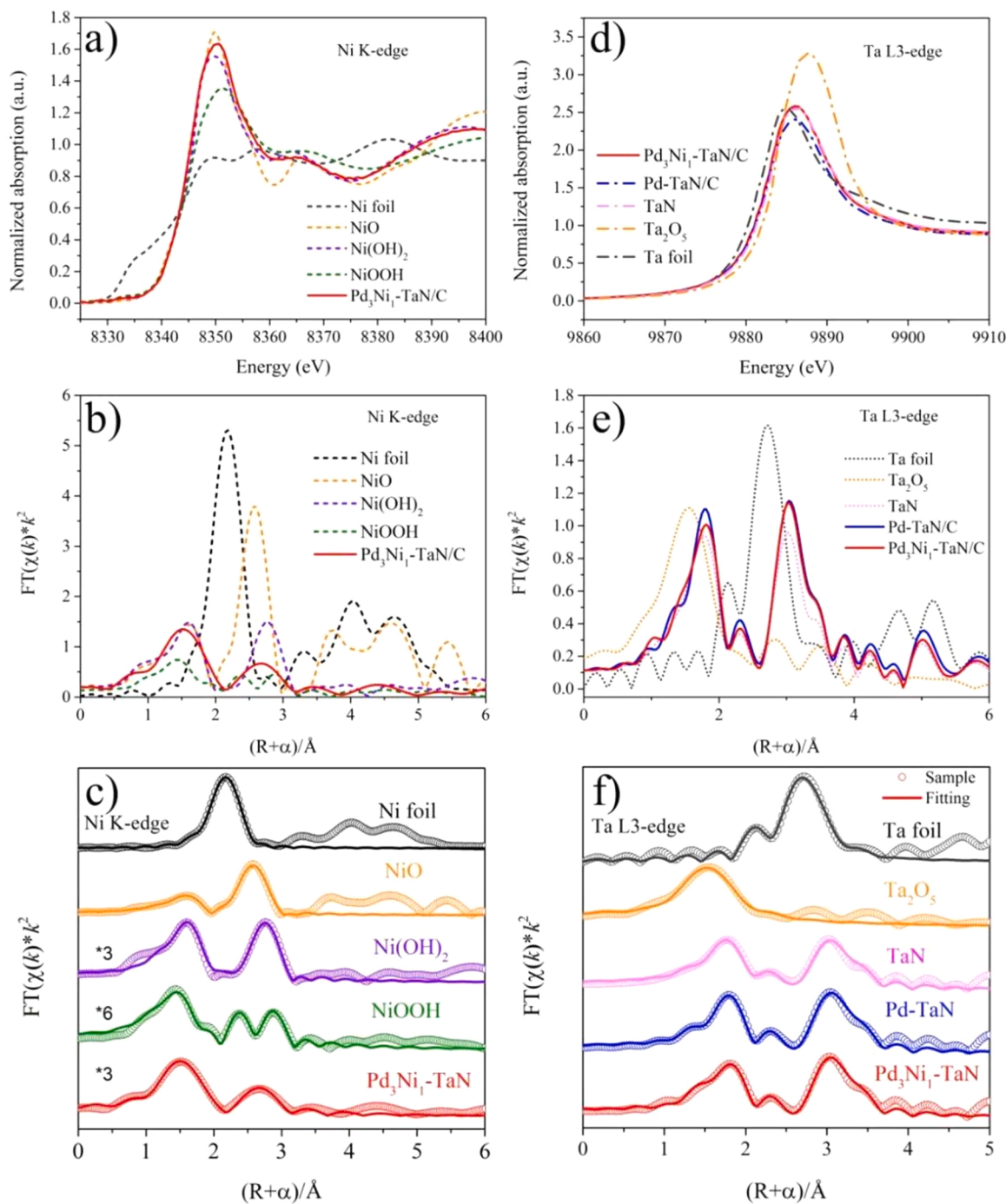


Fig. 4. (a) Normalized XANES spectra of Ni K-edge for Ni foil, NiO, Ni(OH)₂, NiOOH and Pd₃Ni₁-TaN/C catalysts; (b) k^2 -weighted Fourier transform of Ni K-edge EXAFS spectra for Ni foil, NiO, Ni(OH)₂, NiOOH and Pd₃Ni₁-TaN/C catalysts, the data are k^2 -weighted and not phase-corrected; (c) FT of Ni K-edge EXAFS spectra (points represented by circles) and corresponding fitting curves (solid line) for Ni foil, NiO, Ni(OH)₂, NiOOH and Pd₃Ni₁-TaN/C catalysts, the data are k^3 -weighted and not phase-corrected; (d) Normalized XANES spectra of Ta L3-edge for Ta foil, Ta₂O₅, TaN, Pd-TaN/C and Pd₃Ni₁-TaN/C; (e) k^2 -weighted FT of Ta L3-edge EXAFS spectra; (f) FT of Ta L3-edge EXAFS spectra (points represented by circles) and corresponding fitting curves (solid line) for Ta foil, Ta₂O₅, TaN, Pd-TaN/C and Pd₃Ni₁-TaN/C, the data are k^3 -weighted and not phase-corrected.

can be identified. The first peak at around 2 \AA (without phase correction) represents Ta-N distance, and the second peak at around 3 \AA (without phase correction) represents Ta-Ta (or Ta-N-Ta) distance. It is noticeable for Pd₃Ni₁-TaN/C that, there is a slight decrease in the intensity of the Ta-N distance compared with Pd-TaN/C, as demonstrated in Fig. 4(e). It can be suggested that Ta-N coordination number in Pd₃Ni₁-TaN/C decreases after the Ni incorporation, which is supported by the EXAFS fitting results. Quantitatively, the Ta EXAFS fitting results (Table 2, Table S4 and Fig. 4f) suggest that the coordination number of

Ta-N decreases from 4.3 of Pd-TaN/C to 3.1 of Pd₃Ni₁-TaN/C after the introduction of Ni into Pd-TaN/C, indicative of the emergence of nitrogen vacancy in the bulk [68–70]. The reduced contribution of N-Ta in Pd₃Ni₁-TaN/C after incorporating Ni is also supported by the XPS results (contents of N-Ta). The similar Wavelet-transform (WT) analysis of the Ta L3-edge EXAFS spectra for these catalysts is also carried out and shown in Fig. 5(b). Different from the intensity maximum of Ta-Ta path at 8.3 \AA^{-1} for Ta foil and Ta-O path at 3.8 \AA^{-1} for Ta₂O₅, TaN has the WT maximum at a higher k -value of 8.9 \AA^{-1} for the Ta-Ta (or Ta-N-Ta) path

Table 1

Curvefit parameters^a for Ni K-edge EXAFS for Pd₃Ni₁-TaN/C and Pd-TaN-C catalysts.

Materials	Ni-O		Ni-O-Ni		Ni-Ni	
	N	R/Å	N	R/Å	N	R/Å
Ni foil					12	3.0 ± 0.01
NiO	6	2.08 ± 0.01	12	2.95 ± 0.01		
Ni(OH) ₂	6	2.06 ± 0.01	6	3.12 ± 0.01		
NiOOH	6	4	6	2	2.86 ± 0.02	3.06 ± 0.02
		1.96 ± 0.02				
		2.14 ± 0.04				
Pd ₃ Ni ₁ -TaN/ C	6.1 ± 0.9	2.05 ± 0.01	3.1 ± 0.7	3.04 ± 0.01		

^aS₀² was fixed as 0.96.

and a lower k-value of 4.6 Å⁻¹ for the Ta-N path, which is similar to Pd₃Ni₁-TaN/C and Pd-TaN/C. Moreover, compared with Pd-TaN/C, the lower signal of Ta-N path for Pd₃Ni₁-TaN/C further illustrates the generation of nitrogen vacancy [71], consistent with the EXAFS results. In

conclusion, these results indicate that the incorporation of Ni brings more nitrogen vacancies in the Pd₃Ni₁-TaN/C catalyst, implying that the strong interfacial electronic interactions between them occur.

3.2. Electrochemical studies on the Pd₃Ni₁-TaN/C, Pd-TaN/C, Pd₃Ni₁/C and commercial Pd/C catalysts

Firstly, Fig. S6 shows the CV curves of the Pd₃Ni₁-TaN/C, Pd-TaN/C, Pd₃Ni₁/C and commercial Pd/C catalysts in an Ar-saturated 1 M KOH

Table 2

Curvefit parameters^a for Ta L3-edge EXAFS for Pd₃Ni₁-TaN/C and Pd-TaN-C catalysts.

Materials	Ta-N		Ta-N		Ta-Ta		Ta-Ta	
	N	R/Å	N	R/Å	N	R/Å	N	R/Å
TaN	0.9 ±0.6	1.91 ±0.07	4.9 ±1.3	2.14 ±0.02	1.6 ±0.7	2.95 ±0.02	4.1 ±1.8	3.33 ±0.01
Pd/TaN-C	0.9 ±0.4	1.94 ±0.05	4.3 ±0.9	2.15 ±0.02	1.8 ±0.6	2.96 ±0.02	4.1 ±1.6	3.34 ±0.01
Pd ₃ Ni ₁ - TaN/C	1.2 ±0.4	2.02 ±0.05	3.1 ±1.1	2.18 ±0.03	2.1 ±1.4	2.97 ±0.03	4.2 ±2.8	3.34 ±0.01

^aS₀² was fixed as 0.95 on the base of Ta foil.

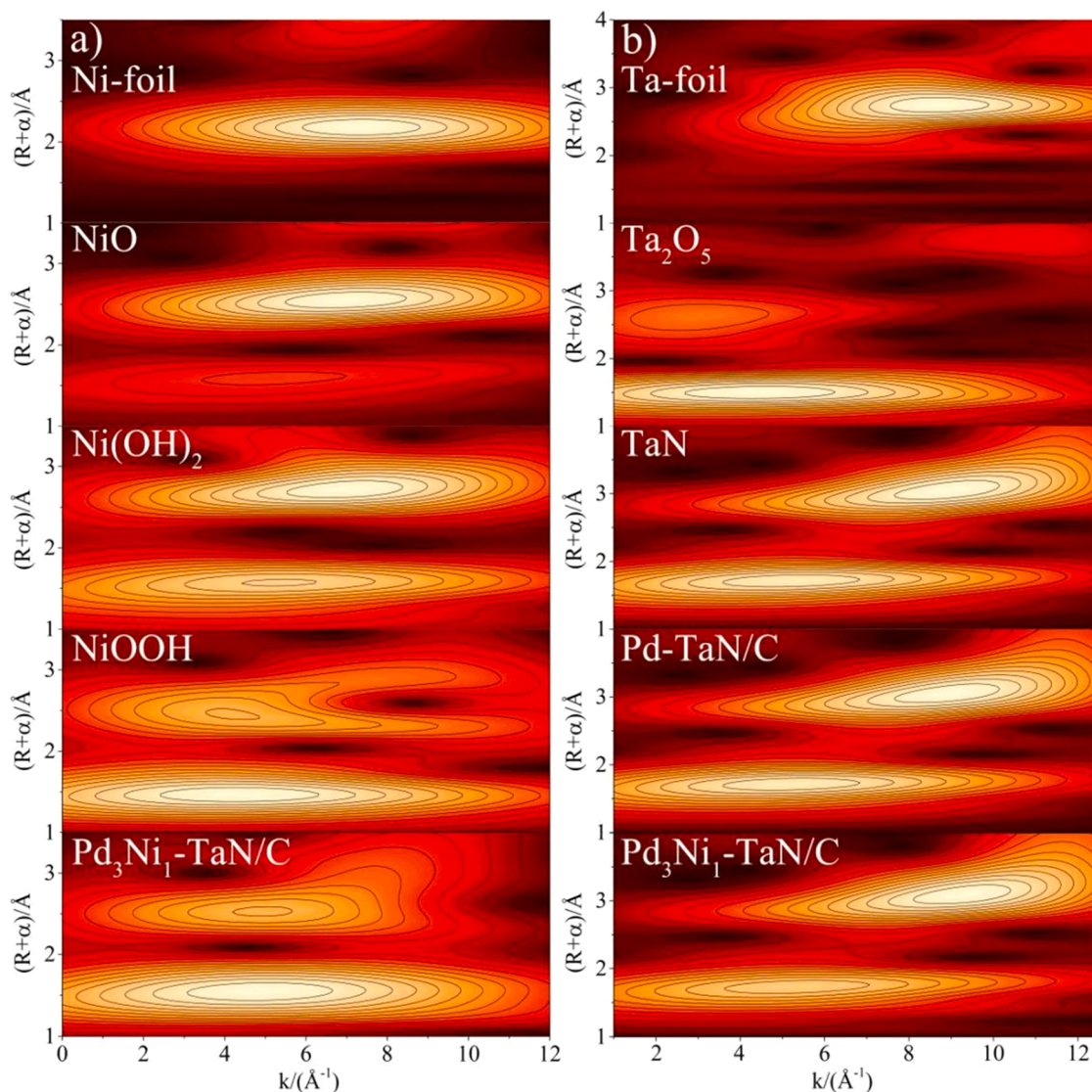


Fig. 5. (a) WT-EXAFS for Ni foil, NiO, Ni(OH)₂, NiOOH and Pd₃Ni₁-TaN/C catalysts; (b) WT-EXAFS for Ta foil, Ta₂O₅, TaN, Pd-TaN/C and Pd₃Ni₁-TaN/C.

solution. As shown in Fig. S6, it consists of three regions: the hydrogen adsorption/desorption peak (0–0.35 V), the double layer charge (0.35–0.55 V) and the formation/reduction of Pd oxide (Pd-OH_{ad} and Pd-O, 0.55–1.4 V) [EES]. The results indicate that the Pd-OH peaks of Pd₃Ni₁-TaN/C have lower onset potentials than that of Pd-TaN/C, Pd₃Ni₁/C and commercial Pd/C catalysts, implying the preferential adsorption of OH after the incorporation of TaN and Ni.

The activity of the Pd₃Ni₁-TaN/C, Pd-TaN/C and the reference catalysts (Pd₃Ni₁/C and commercial Pd/C) for MOR are examined in Ar-purged 1 M CH₃OH with 1 M KOH. As shown in Fig. 6(a), typical CV curves corresponding to the electro-oxidation of methanol in the forward (anodic, from 0 V to 1.4 V) and reverse (cathodic, from 1.4 to 0 V) scans based on the mass of Pd are recorded at 50 mV s⁻¹. The anodic peak in the forward scan can be attributed to the oxidation of the

absorbed methanol and the cathodic peak in the reverse scan is ascribed to the oxidation of carbonaceous intermediates which are not oxidized completely in the forward scan.

Fig. 6(b) shows the peak potential activity (indicating the height of these peak) of the Pd₃Ni₁-TaN/C, Pd-TaN/C, Pd₃Ni₁/C and commercial Pd/C catalysts, which reflects the catalytic activity. The mass activities of Pd₃Ni₁-TaN/C, Pd-TaN/C and Pd₃Ni₁/C catalysts towards alkaline MOR are normalized by the actual content of Pd loading (Table S1) in this work. The Pd₃Ni₁-TaN/C catalyst exhibits much higher current density of 3636.36 A g_{Pd}⁻¹ in comparison to other catalysts (1913.88 A g_{Pd}⁻¹ for Pd-TaN/C, 1244.02 A g_{Pd}⁻¹ for Pd₃Ni₁/C and 210.53 A g_{Pd}⁻¹ for commercial Pd/C). It is noticeable that, the mass activity of Pd₃Ni₁-TaN/C towards MOR in alkaline medium is 14 times that of the reported commercial PtRu/C (260 A g_{Pd}⁻¹) [72]. The comparison of catalytic

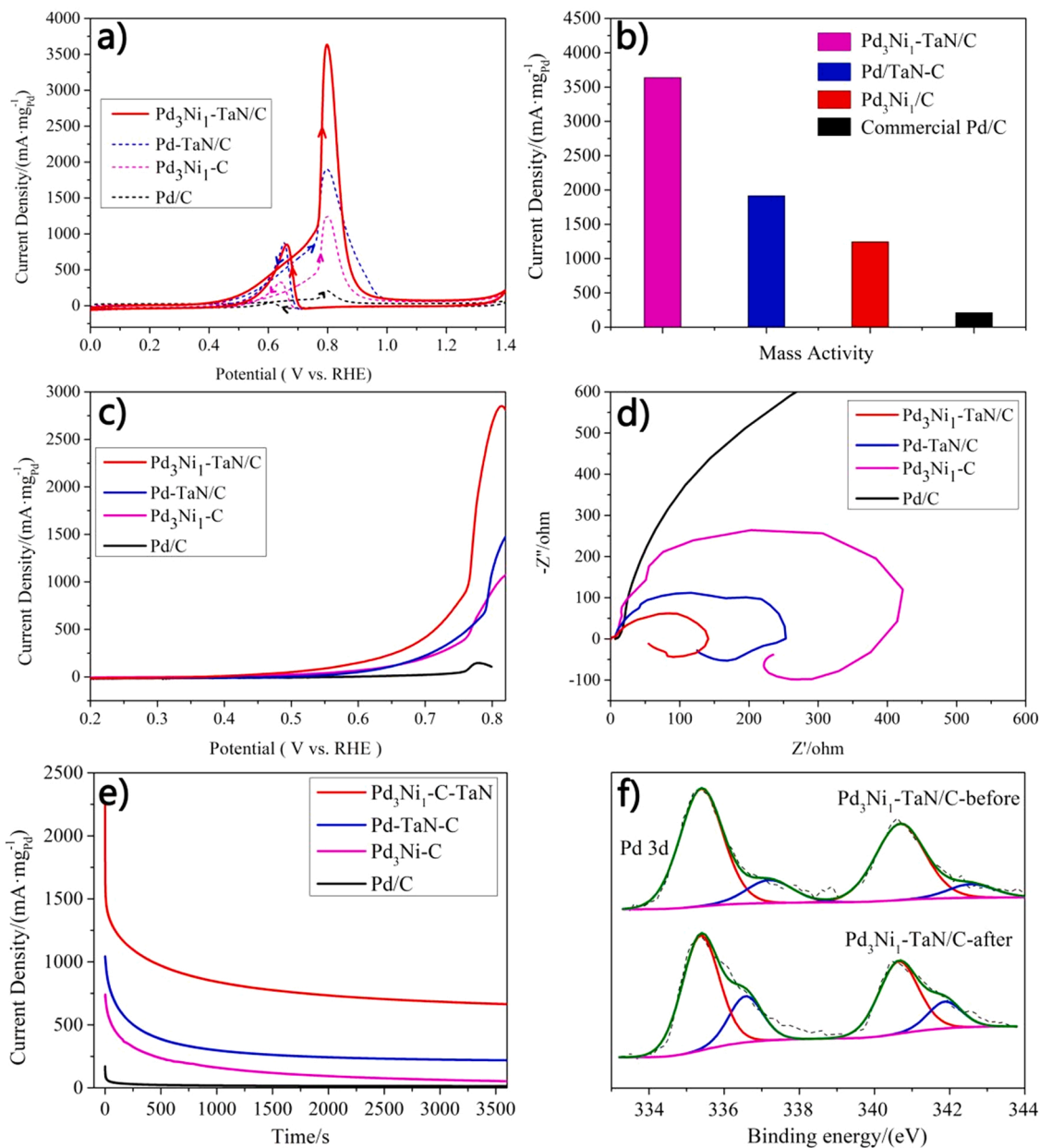


Fig. 6. (a) CV curves of Pd₃Ni₁-TaN/C, Pd-TaN/C, Pd₃Ni₁/C and commercial Pd/C catalysts in Ar-saturated 1 M CH₃OH and 1 M KOH with a sweep rate of 50 mV s⁻¹ (The arrow suggests the corresponding part in each plot to forward scan and backward scan, respectively); (b) the peak potential activity of Pd₃Ni₁-TaN/C, Pd-TaN/C, Pd₃Ni₁/C and commercial Pd/C catalysts in Ar-saturated 1 M CH₃OH and 1 M KOH; (c) LSV curves of Pd₃Ni₁-TaN/C, Pd-TaN/C, Pd₃Ni₁/C and commercial Pd/C catalysts in Ar-saturated 1 M CH₃OH and 1 M KOH with a sweep rate of 5 mV s⁻¹; (d) the corresponding EIS plots of Pd₃Ni₁-TaN/C, Pd-TaN/C, Pd₃Ni₁/C and commercial Pd/C in Ar-saturated 1 M CH₃OH and 1 M KOH at 0.76 V vs RHE; (e) CA curves of Pd₃Ni₁-TaN/C, Pd-TaN/C, Pd₃Ni₁/C and commercial Pd/C catalysts in Ar-saturated 1 M CH₃OH and 1 M KOH at 0.76 V vs RHE; (f) High-resolution Pd 3d of XPS spectra of the Pd₃Ni₁-TaN/C catalysts for pre- and post-MOR in alkaline media.

performance of other Pd-based catalysts reported recently towards MOR in alkaline medium are also listed in Table S5 in Supporting Information. Additionally, as listed in Table 3, the Pd₃Ni₁-TaN/C catalyst (137.75 m² g⁻¹) also exhibits the larger ECSA relative to Pd-TaN/C (85.62 m² g⁻¹), Pd₃Ni₁/C (53.43 m² g⁻¹) and commercial Pd/C (42.23 m² g⁻¹), which is obtained by the integral area of CO oxidation peak by CO stripping technique. This result suggests that Pd₃Ni₁-TaN/C has more exposed active sites in comparison with other catalysts, possibly due to the unsaturated coordination environment of Pd₃Ni₁-TaN/C (including the combination of highly dispersed Ni and nitrogen defects) demonstrated by HAADF STEM and EXAFS results. The large ECSA of the Pd₃Ni₁-TaN/C catalyst is also responsible for the enhanced catalytic performance of MOR in alkaline medium. Meanwhile, the Pd₃Ni₁-TaN/C catalyst shows the highest specific activity (normalized by ECSA) of 2.64 mA cm⁻² among the Pd-TaN/C (2.23 mA cm⁻²), Pd₃Ni₁/C (2.32 mA cm⁻²) and commercial Pd/C (0.49 mA cm⁻²) catalysts. The result suggests that the Pd₃Ni₁-TaN/C catalyst have the highest intrinsic activity among all the catalysts, which can be attributed to effective active sites and optimal electronic structures in Pd₃Ni₁-TaN/C along with core-shell-like morphology, demonstrated by above HAADF-STEM, XPS and EXAFS results.

To gain insight into the reaction kinetics, LSV and EIS measurements are carried out, as shown in Fig. 6(c-d). It is observed that the onset potentials in LSV curves of the Pd₃Ni₁-TaN/C, Pd-TaN/C, Pd₃Ni₁/C and commercial Pd/C catalysts corresponds to 0.44 V, 0.53 V, 0.52 V and 0.62 V, respectively. The most negative-shifted onset potential of the Pd₃Ni₁-TaN/C catalyst indicates the promoting MOR kinetic properties to oxidize methanol in alkaline medium. The charge transfer kinetics on the surface are further evaluated by the EIS technique (Fig. 6d). It is observed that the Pd₃Ni₁-TaN/C catalyst exhibits the smallest semi-circular diameters among all the catalysts, suggesting the decreased interfacial resistance and rapid charge transfer towards MOR in alkaline medium. The results indicate the combination of TaN and Ni(OH)₂/NiOOH effectively facilitates the charge transfer kinetics at the interface during the alkaline media.

To evaluate the long-term stability of catalysts of MOR in alkaline medium, CA measurements are conducted at 0.76 V vs RHE for 3600 s in Ar-purged 1 M CH₃OH with 1 M KOH, as shown in Fig. 6(e). For all the samples, it can be found that the current densities of catalysts drop rapidly due to the accumulated intermediates in the first stage. Then the current densities of catalysts almost maintain the steady state. Compared with other catalysts, it is observed that Pd₃Ni₁-TaN/C always exhibits higher current densities in the initial stage and the later stage, suggesting that it has higher anti-poisoning ability and catalytic durability towards MOR in alkaline medium. The retained mass activity after i-t testing has been summarized in Fig. S7. Furthermore, as shown in Fig. S8, the mass activity of Pd₃Ni₁-TaN/C maintains 88% of the original activities after 200 CV cycles, while 82%, 70% and 58% of the initial performance maintain for the Pd-TaN/C, Pd₃Ni₁/C and commercial Pd/C. This result suggests that Pd₃Ni₁-TaN/C shows improved MOR durability in comparison with other catalysts. Additionally, to deeply gain insight into the structural stability of the Pd₃Ni₁-TaN/C catalyst, the Pd 3d measured by XPS techniques for pre-MOR and post-MOR in alkaline medium is also investigated. As shown in Fig. 6f, it is found that there is

no obvious shift of binding energy and only a slight increase of the oxidized Pd, mainly from the surface oxidation, suggesting that the structural stability of the Pd₃Ni₁-TaN/C catalyst is well maintained after MOR in alkaline medium.

In conclusion, electrochemical results demonstrate that, compared with Pd-TaN/C and other reference catalysts, Ni incorporation into Pd₃Ni₁-TaN/C catalyst not only elevates the catalytic activity and kinetics, but also presents the outstanding catalytic activity durability and structural stability, confirming Pd₃Ni₁-TaN/C catalyst to be an excellent anode catalysts for alkaline MOR.

3.3. In situ ATR-SEIRAS observation of MOR in alkaline media

For the purpose of elucidating the reaction pathway and deducing reaction mechanism to provide a molecule-level understanding of the outstanding catalytic performance of Pd₃Ni₁-TaN/C, in situ ATR-SEIRAS technique is further employed to track the adsorbed intermediates and products. Fig. 7 presents the in situ ATR-SEIRAS spectra recorded between 4000 and 1290 cm⁻¹ at the applied voltage in the range of 0–1.4 V during the alkaline MOR testing process on the Pd₃Ni₁-TaN/C and Pd-TaN/C catalysts. The in situ ATR-SEIRAS spectra of commercial Pd/C can be found in our previous report [14].

As observed in Fig. S9, the bands at 1050 cm⁻¹ are attributed to C-O stretching vibrations of CH₃OH and/or CH₃O species [73–75]. Fig. 7(a, c) presents the in situ ATR-SEIRAS spectra between 4000 and 3000 cm⁻¹, in which the band near 3000 cm⁻¹ is attributed to the C-H stretching vibrations of CH₃OH and/or CH₃O species, and the band near 3600 cm⁻¹ is attributed to the OH stretching vibrations [74,76,77]. The band at 1580 cm⁻¹ in Fig. 7(b, d) is the peak for the asymmetric stretching vibration of HCOO_{ad} [76, 78–81], indicating that HCOO_{ad} is the intermediate of alkaline MOR on the Pd₃Ni₁-TaN/C and Pd-TaN/C catalysts, which is different from commercial Pd/C catalyst where no HCOO_{ad} peak is detected in our previous work [14]. The band at 1620 cm⁻¹ in Fig. 7(b, d) is attributed to the stretching deformations of water molecules, whose intensities are so strong that the bands (such as the C=O stretching vibration or the HCO₃ bands) between 1600 and 1800 cm⁻¹ are affected [75,78,79,82]. In addition, the peaks for CO species (including multi-bonded CO, bridge-bonded CO and linear-bound CO bands) are not detected on the Pd₃Ni₁-TaN/C and Pd-TaN/C catalysts. The missing CO peaks indicate that CO species are not the main intermediates with high coverage on the Pd₃Ni₁-TaN/C and Pd-TaN/C catalysts, or that CO species can be removed rapidly on their surfaces [83]. The detailed frequencies and assignments of the in situ ATR-SEIRAS bands are summarized in Table 4.

To gain insight on the possible reaction mechanism, quantitative comparisons of integrated intensities of HCOO_{ad} and CO bands on the Pd₃Ni₁-TaN/C, Pd-TaN/C and commercial Pd/C catalysts with the applied voltage in the range of 0–1.4 V are performed, as shown in Fig. 8 (a, b). Obviously, as observed in Fig. 8(a), HCOO_{ad} band shows the high intensity on Pd₃Ni₁-TaN/C, low intensity on Pd-TaN/C and no intensity on the commercial Pd/C catalyst at applied voltages. Also, the onset potential for the formation of HCOO_{ad} bands on Pd₃Ni₁-TaN/C (0.58 V) is lower than that on Pd-TaN/C (0.85 V), indicating that the presence of Ni promotes the formation of HCOO_{ad}. Taken together, the formation of HCOO_{ad} intermediates during methanol oxidation reaction in alkaline medium on the Pd-based catalysts is very sensitive to the presence of TaN, which can be further facilitated by adding a second metal of Ni, similar to the previous reports [14]. Besides, as observed in Fig. 8(b), CO band presents high intensity only on commercial Pd/C and no intensity on the Pd₃Ni₁-TaN/C and Pd-TaN/C catalysts. Therefore, it can be proposed that methanol oxidation on commercial Pd/C occurs through CO pathway, and methanol oxidation on the Pd₃Ni₁-TaN/C and Pd-TaN/C catalysts occurs via HCOO_{ad} pathway.

Furthermore, combined with the MOR activities and the HCOO_{ad} results of in situ ATR-SEIRAS analysis, it is also found that, on the Pd₃Ni₁-TaN/C and Pd-TaN/C catalysts, the voltage-dependence of the

Table 3

The catalytic performance of Pd₃Ni₁-TaN/C, Pd-TaN/C, Pd₃Ni₁/C, TaN-C and commercial Pd/C towards MOR in alkaline medium.

Materials	ECSA (m ² g ⁻¹)	MOR	
		I _p (m) (A g _{Pd} ⁻¹)	I _p (sa) (mA cm _{Pd} ⁻²)
Pd ₃ Ni ₁ -TaN/C	137.75	3636.36	2.64
Pd-TaN-C	85.62	1913.88	2.23
Pd ₃ Ni ₁ /C	53.43	1244.02	2.32
TaN-C	0	0	0
Commercial Pd/C	42.23	210.53	0.49

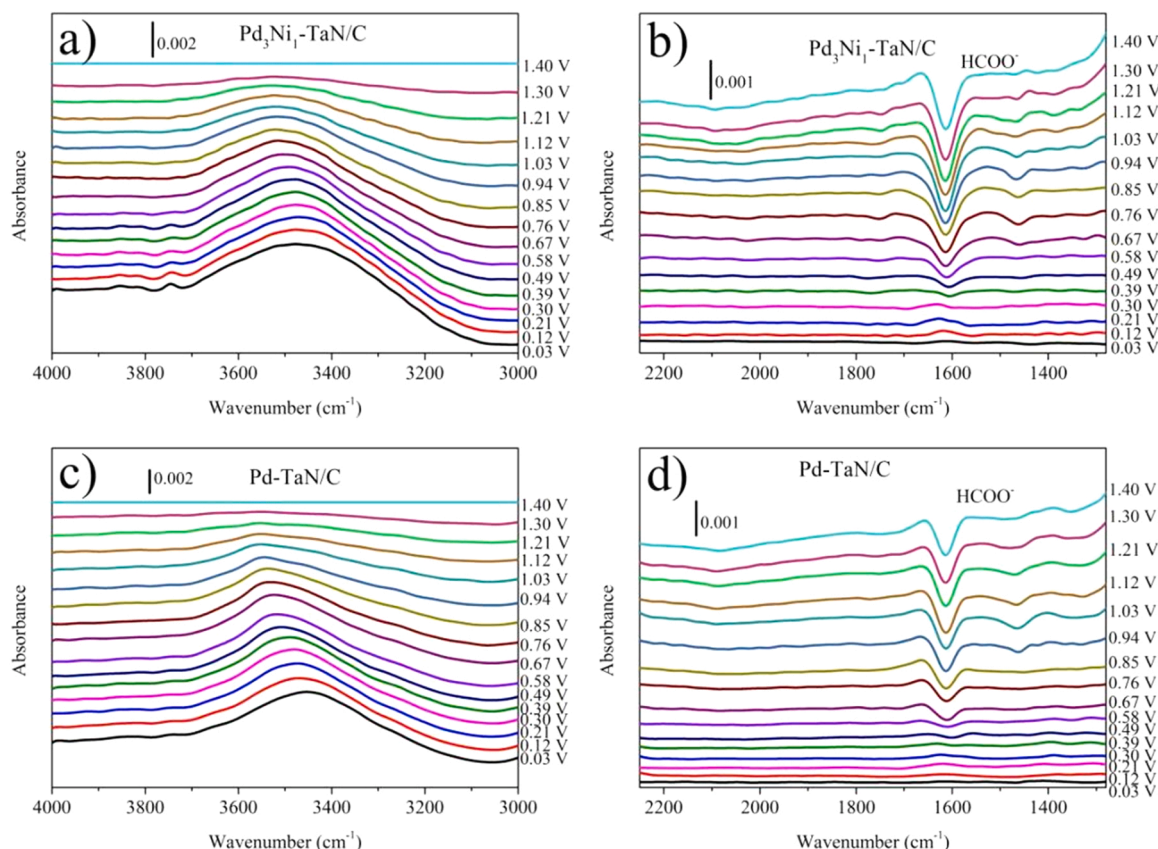


Fig. 7. *In situ* ATR-SEIRAS spectra on the Pd₃Ni₁-TaN/C (a, b) and Pd-TaN/C catalysts (c, d) at the applied voltage in the range of 0–1.4 V for MOR in 1 M CH₃OH and 1 M KOH.

Table 4

Assignments of *in situ* ATR-SEIRAS spectra observed in Fig. 7.

Wavenumbers (cm ⁻¹)	Assignments
~1050	ν (C-O) of surface CH ₃ OH and/or CH ₃ O
~1440	δ (C-H) of surface CH ₃ OH and/or CH ₃ O
~1580	ν (OCO) of asymmetric HCOO _{ad}
~1650	δ (H-O-H) of interfacial H ₂ O
2500–3000	ν (C-H) of adsorbed CH ₃ OH and/or CH ₃ O
3000–3700	ν (O-H) of interfacial water

ν , stretching vibration; δ , bending vibration.

HCOO_{ad} integrated intensities matches well with that of the catalytic activities, implying that HCOO_{ad} may be a vital intermediate during MOR in alkaline media, which is in accord with previous reports [84, 85]. It has been reported that HCOO_{ad} will promote the splitting of C-H and thus facilitate the generation of CO₂ with a low activation energy [84–86]. Additionally, relative to commercial Pd/C catalysts, the higher catalytic current densities of the Pd₃Ni₁-TaN/C and Pd-TaN/C catalysts can also be explained by the lack of the accumulation of CO species, which are considered to be poisoning intermediates due to the strong absorption ability of CO species on the surface makes it hard to release the active sites for further oxidation [20,87,88].

Besides the possible intermediates mentioned above, the features of interfacial water molecule between 4000 and 3000 cm⁻¹ are also investigated quantitatively and qualitatively by the *in situ* ATR-SEIRAS to provide more molecular-level evidence for further verification of the catalysts' anti-CO poisoning ability and durability, as shown in Fig. 8(c, d). The detailed fitting results can be found in the Supporting information (Fig. S10–S12, Table S6–S7). Based on the published reports, the fitting bands at 3270 cm⁻¹, 3450 cm⁻¹ and 3600 cm⁻¹ are attributed to tetrahedrally coordinated water (water molecules with strong H-bonds),

trihedrally coordinated water (water molecules with weak H-bonds) and the dangling O-H stretching vibration (water molecules with non H-bonds) [14, 77, 89–92]. It has been reported that OH can react with CO, thus facilitating the removal of CO on the surface on the base of the bi-functional theory (i.g. Langmuir-Hinshelwood (H-L) mechanism, Eley-Rideal mechanism (E-L) mechanism) [14,84,93]. Therefore, the band at 3600 cm⁻¹ representing dangling O-H stretching vibration is the focus in the work. As observed in Fig. 8(c, d), from a quantitative and qualitative point of view, Pd₃Ni₁-TaN/C presents both a higher OH intensity and a higher OH percentage than those of Pd-TaN/C and commercial Pd/C catalysts at all applied voltages. It is also found that, relative to commercial Pd/C catalyst, OH bands are facile to generate on Pd₃Ni₁-TaN/C and Pd-TaN/C during MOR in alkaline medium, indicating that the presence of TaN is beneficial to the OH formation, which can explain the absence of CO bands on the Pd₃Ni₁-TaN/C and Pd-TaN/C catalysts during the alkaline MOR by the bi-functional theory. Meanwhile, Pd₃Ni₁-TaN/C also exhibits a higher OH intensity and a higher OH percentage than those of Pd-TaN/C catalyst, suggesting that the presence of Ni also favors the OH formation, which may be due to the high oxophilicity feature of Ni [14,84,94]. Combining the MOR activities and the *in situ* ATR-SEIRAS results (including CO bands and OH bands), it can be concluded that the additions of both TaN and Ni facilitate the OH formation, thereby accelerating the oxidation removal of the poisoning intermediates such as CO, which can also explain the promoted catalytic performance of Pd₃Ni₁-TaN/C relative to Pd-TaN/C and commercial Pd/C catalysts.

Taken together, for the commercial Pd/C catalyst, MOR occurs only through the CO pathway, whereas for the Pd-TaN/C catalyst, MOR proceeds only through the HCOO_{ad} pathway, indicating that TaN helps to undergo the HCOO_{ad} pathway during the alkaline MOR. Relative to the Pd-TaN/C catalyst, the Pd₃Ni₁-TaN/C catalyst will generate a

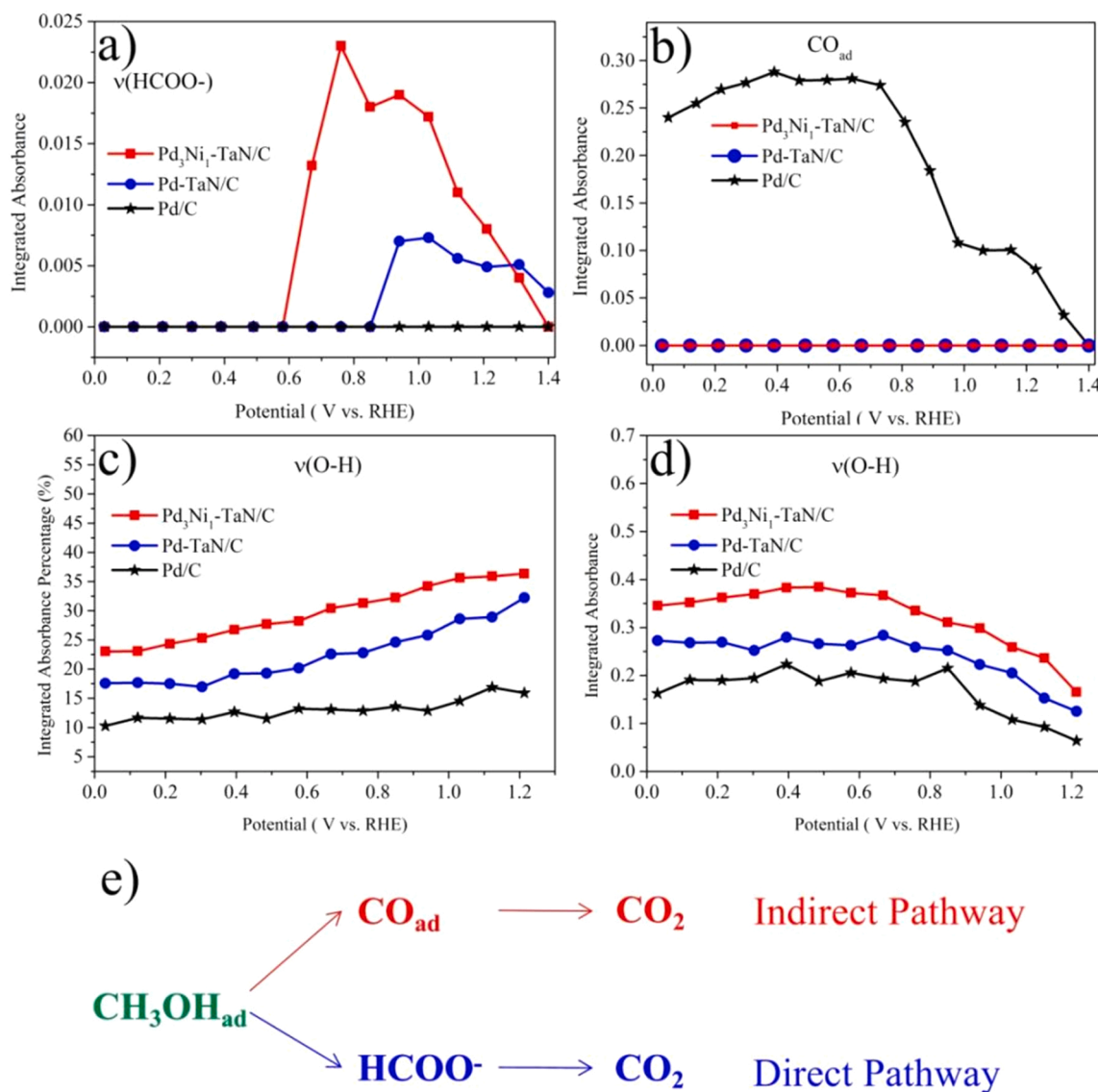


Fig. 8. Integrated in situ ATR-SEIRAS band intensities of HCOO_{ad} (a), CO (b), OH percentage (c) and OH (d) at the applied voltage during the alkaline MOR testing process on the $\text{Pd}_3\text{Ni}_1\text{-TaN/C}$, Pd-TaN/C catalysts and commercial Pd/C catalysts. Proposed MOR reaction mechanism in alkaline media (e).

relatively large amount of HCOO_{ad} and OH during the alkaline MOR, indicating that Ni can further promote the HCOO_{ad} route and enhance the OH adsorption. According to the above analysis, it can be proposed that MOR on commercial Pd/C occurs through CO pathway in alkaline media, and MOR on the $\text{Pd}_3\text{Ni}_1\text{-TaN/C}$ and Pd-TaN/C catalysts occurs via HCOO_{ad} pathway in alkaline media, as shown in Fig. 8(e).

3.4. DFT calculations

DFT calculations are used to further confirm in situ ATR-SEIRAS and electrochemical results and study the effect of OH on the catalytic performance for MOR. According to the above EXAFS and XPS results, the models are constructed and shown in Fig. 9 and Fig. S13-S14. However, the evident difference exists between the models and the real catalysts. Using the $\text{Pd}_3\text{Ni}_1\text{-TaN/C}$ catalyst as an example, the nanoparticle sizes, morphologies and spatial distributions of the components of the real catalysts are simplified at some extent. Besides, different Ni species from XPS analysis are modeled by the sole $\text{Ni}(\text{OH})_2$ component due to the highest proportion, similar to TaN. The special core/shell-like structure provided by TaN/C and the effect from various valence state of Ni is ignored. The distribution, number and concentration information of

nitrogen vacancies are also simplified. Considering the computational accuracy and period, the real catalysts are substituted by the corresponding models in Fig. S1 and Fig. 9, which is agreement with our previous studies [14,20].

The binding energies of CH_3OH , CO and OH are calculated on the Pd (111), $\text{Pd}_4/\text{TaN}(001)$, $\text{Pd}_4\text{-Ni}(\text{OH})_2\text{-TaN}(001)$ and $\text{Pd}_4\text{-Ni}(\text{OH})_2\text{-TaN}(001)\text{-V}$ surfaces, listed in the Table 5. The corresponding adsorption configurations are shown in Fig. 9a and Fig. S13-S14. Based on our previous studies [9], it is suggested that TaN helps to enhance the CO_{ad} removal at some extent compared to Pd(111). In this section, the effect of Ni species will be discussed. Firstly, it is indicated that the introduction of $\text{Ni}(\text{OH})_2$ enhances the interaction between CH_3OH and Pd/TaN surface, which is beneficial for the activation of methanol molecules. Besides, the CO binding energy is reduced evidently on the $\text{Pd}_4\text{-Ni}(\text{OH})_2\text{-TaN}(001)\text{-V}$ surface, indicating that the existence of Ni (OH)₂ improve its CO tolerance compared with Pd(111) and $\text{Pd}_4/\text{TaN}(001)$, consistent with the in situ ATR-SEIRAS results that non-CO is detected. Furthermore, the effect of nitrogen vacancy is studied. As shown in Fig. 9 and Table 5, compared with $\text{Pd}_4\text{-Ni}(\text{OH})_2\text{-TaN}(001)$, it can be found that the abilities of methanol activation and CO tolerance are enhanced significantly on the $\text{Pd}_4\text{-Ni}(\text{OH})_2\text{-TaN}(001)\text{-V}$ surface. The

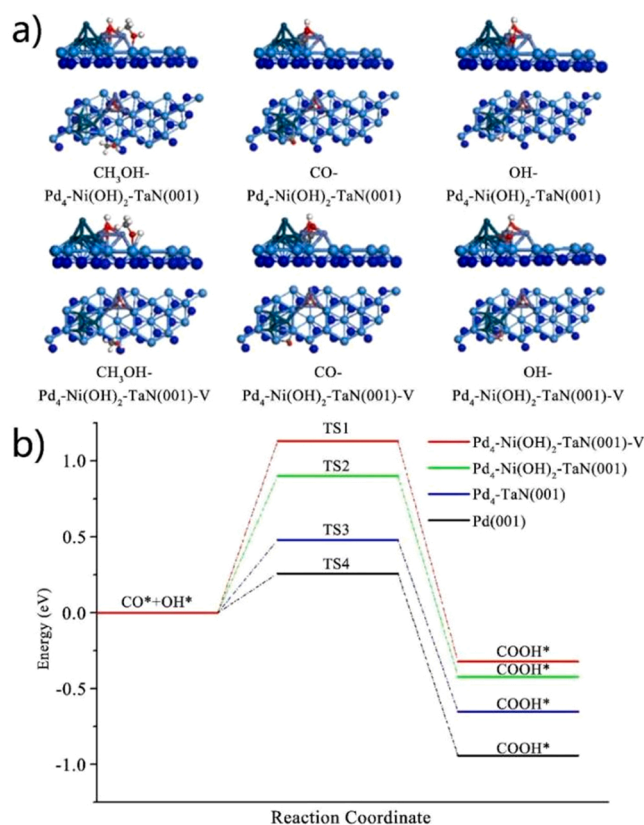


Fig. 9. a) The optimized adsorption configurations of the corresponding species on the $\text{Pd}_4\text{-Ni(OH)}_2\text{-TaN(001)}$ and $\text{Pd}_4\text{-Ni(OH)}_2\text{-TaN(001)-V}$ surfaces. b) The potential energy profiles $\text{CO}_{\text{ad}} + \text{OH}_{\text{ad}}$ to COOH_{ad} on the Pd(111) , $\text{Pd}_4\text{-TaN(001)}$, $\text{Pd}_4\text{-Ni(OH)}_2\text{-TaN(001)}$ and $\text{Pd}_4\text{-Ni(OH)}_2\text{-TaN(001)-V}$ surfaces.

Table 5

DFT calculated binding energies of CH_3OH , CO and OH on the Pd(111) , $\text{Pd}_4\text{-TaN(001)}$, $\text{Pd}_4\text{-Ni(OH)}_2\text{-TaN(001)}$ and $\text{Pd}_4\text{-Ni(OH)}_2\text{-TaN(001)-V}$ surfaces.

Species	Binding energy (eV)			
	Pd (111)	$\text{Pd}_4\text{-TaN(001)}$	$\text{Pd}_4\text{-Ni(OH)}_2\text{-TaN(001)}$	$\text{Pd}_4\text{-Ni(OH)}_2\text{-TaN(001)-V}$
CH_3OH	-0.27	-0.69	-1.13	-1.58
CO	-2.18	-1.36	-0.43	-0.27
OH	-2.26	-3.86	-4.88	-5.76

adsorption energies of CH_3OH and CO are -1.58 and -0.27 eV, suggesting that the presence of nitrogen vacancy can promote the catalytic activity for MOR, consistent with the CV, LSV, CA, Tafel results.

As we all know, increasing the anti-CO poisoning ability is important for the durability and stability of Pd-based catalysts for MOR. The in situ ATR-SEIRAS results indicate that the co-adsorbed hydroxyl concentration is highest on the PdNi-TaN catalyst surface, which can facilitate the removal of adsorbed CO . To confirm the effect of OH on the CO_{ad} conversion, the OH binding energies and the energy barriers of COOH formation are calculated on different surfaces. The adsorption configurations and potential energy profiles $\text{CO}_{\text{ad}} + \text{OH}_{\text{ad}}$ to COOH_{ad} are shown in Fig. 9(a-b). The DFT-calculated activation barriers and reaction energies of the corresponding reaction are listed in Table S8. Compared with $\text{Pd}_4\text{-TaN(001)}$, it can be found that the binding energy of OH is enhanced evidently after the introduction of Ni(OH)_2 species on the $\text{Pd}_4\text{-Ni(OH)}_2\text{-TaN(001)}$ surface (-4.88 eV). Similarly, the introduction of nitrogen vacancies also strengthens the interaction between OH and catalyst surface on $\text{Pd}_4\text{-Ni(OH)}_2\text{-TaN(001)-V}$ with the binding energy of -5.76 eV. The result is consistent with the high OH

concentration in situ ATR-SEIRAS analysis. Then, to confirm the CO_{ad} removal origin by the OH_{ad} species, the energy barriers of the formation COOH from the reaction $\text{CO} + \text{OH}$ on different surfaces. It is found that the energy barrier is 0.48 eV on the $\text{Pd}_4\text{-Ni(OH)}_2\text{-TaN(001)}$ surface, lower than the value of 0.90 eV on $\text{Pd}_4\text{-TaN(001)}$, suggesting that the introduction of Ni(OH)_2 promotes the formation of COOH and removal of CO_{ad} . Compared with $\text{Pd}_4\text{-Ni(OH)}_2\text{-TaN(001)}$, it is indicated that only 0.26 eV barrier needs to overcome with existence of nitrogen vacancies on the $\text{Pd}_4\text{-Ni(OH)}_2\text{-TaN(001)-V}$ surface, implying that the nitrogen vacancies enhance the conversion of adsorbed CO . The results are also agreements with the in situ ATR-SEIRAS and electrochemical characterizations. In a word, DFT calculations indicate that the introduction of Ni species, TaN and nitrogen vacancies are beneficial for the catalytic performance for alkaline MOR.

3.5. Brief discussion

Notably, TaN/C exhibits no catalytic performance in the absence of Pd catalyst (Fig. S15) and $\text{Pd}_3\text{Ni}_1/\text{C}$ only shows poor catalytic performance ($1244.02 \text{ A g}_{\text{Pd}}^{-1}$) towards MOR in alkaline medium, but $\text{Pd}_3\text{Ni}_1\text{-TaN/C}$ performs excellent MOR activity ($3636.36 \text{ A g}_{\text{Pd}}^{-1}$). Thus, it can be inferred that the true active sites of $\text{Pd}_3\text{Ni}_1\text{-TaN/C}$ to oxidize methanol in alkaline medium come from the synergistic effect of Ni and TaN on the Pd catalyst, that is, the effective construction of PdNi-TaN interface confirmed by XPS and EXAFS characterizations. To make sense the respective roles of Ni and TaN in improving the catalytic performance is of great significance for the rational design of efficient catalysts and is helpful to understand the enhancement mechanism for alkaline MOR.

For one thing, the outstanding catalytic performance of $\text{Pd}_3\text{Ni}_1\text{-TaN/C}$ can be attributed to the structural advantages induced by Ni and TaN . The abundant surface defect sites (i.g. Ni defects and nitrogen vacancies) and the core-shell like morphology of $\text{Pd}_3\text{Ni}_1\text{-TaN/C}$ brings fruitful active sites and unique electronic environment, which presents a crucial effect on the catalytic performance for alkaline MOR, as revealed by electrochemical results, XPS and EXAFS characterizations analysis. For the active sites, ECSA on $\text{Pd}_3\text{Ni}_1\text{-TaN/C}$ is almost twice that of Pd-TaN/C catalyst, in agreement with the difference in their catalytic activities. Additionally, to further reveal the intrinsic electronic structures that are related to the origin of MOR activity and quantify electronic interactions, XPS valence band technique is carried out to measure the valence band electronic structures or the d-orbital electronic configurations of various catalysts. Based on the valence band spectrum subtracted by a Shirley background [95,96], the d-band centers are obtained similar to our previous reports [97]. As shown in Fig. 10(a), the d-band centers of the $\text{Pd}_3\text{Ni}_1\text{-TaN/C}$, Pd-TaN/C and $\text{Pd}_3\text{Ni}_1/\text{C}$ catalysts are -4.51 eV, -4.37 eV and -4.31 eV towards Fermi level, respectively. Compared with the Pd-TaN/C and $\text{Pd}_3\text{Ni}_1/\text{C}$ catalysts, the downshifted d-band center of $\text{Pd}_3\text{Ni}_1\text{-TaN/C}$ further indicates the strong electronic interaction. Moreover, according to the d-band theory, the most negative-shifted d-band center of $\text{Pd}_3\text{Ni}_1\text{-TaN/C}$ catalysts after the incorporation of Ni relative to the Fermi level also implies weaker adsorption of intermediates (such as CO -like poisoning intermediates), which may bring the high catalytic activity and anti-poisoning ability for MOR in alkaline medium. CO -stripping tests are also conducted to verify the enhanced anti-poisoning ability. As shown in Fig. 10(b) and Fig. S16, the $\text{Pd}_3\text{Ni}_1\text{-TaN/C}$ catalyst exhibits the lowest onset potential of CO oxidation among all the catalysts, which follows the trend of $\text{Pd}_3\text{Ni}_1\text{-TaN/C} < \text{Pd-TaN/C} < \text{Pd}_3\text{Ni}_1/\text{C} < \text{commercial Pd/C}$, indicating that CO is easily oxidized on the $\text{Pd}_3\text{Ni}_1\text{-TaN/C}$ catalyst. In other words, $\text{Pd}_3\text{Ni}_1\text{-TaN/C}$ shows the most optimal anti-CO poisoning ability in comparison with other catalysts. This may be due to the hydroxyl adsorption is facile on Ni oxide/hydroxide species verified by the in situ ATR-SEIRAS results, which can oxidize CO -like species and further facilitate MOR performance by means of the bi-functional theory (i.g. Langmuir-Hinshelwood (H-L) mechanism, Eley-Rideal mechanism (E-L) mechanism) [98]. In addition, the absence of CO intermediates in situ

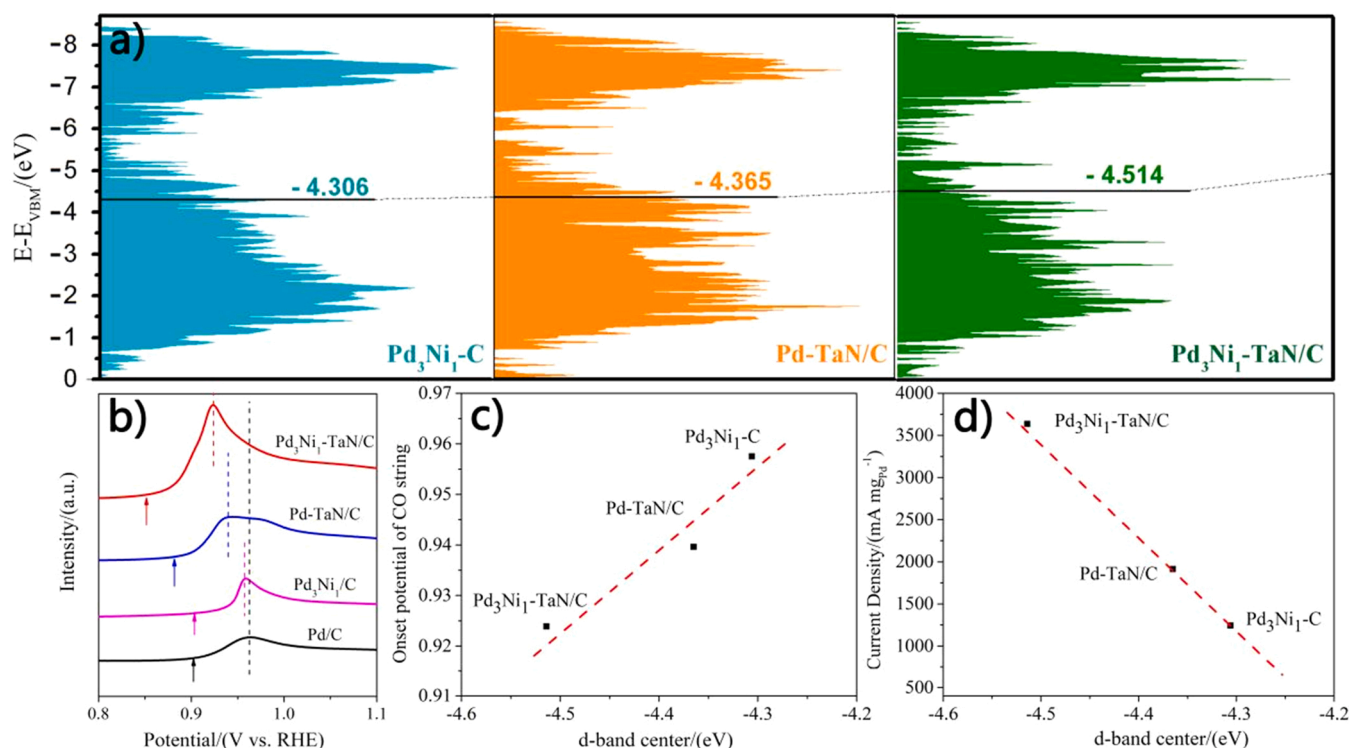


Fig. 10. (a) High-resolution valence band of different bimetallic $\text{Pd}_x\text{Ni}_y\text{-TaN/C}$ to VBM, which is proportional to the DOS. The black solid line represents the d-band center. (b) The corresponding CO stripping plots of $\text{Pd}_x\text{Ni}_y\text{-TaN/C}$ towards methanol oxidation reaction in 0.5 M H_2SO_4 solution. (c) d-band center as a function for the onset potential of CO stripping. Dashed line represents an approximate linear fitting. (d) d-band center as a function for the catalytic activity of $\text{Pd}_x\text{Ni}_y\text{-TaN/C}$ towards MOR in alkaline media. The dashed line represents an approximate linear fitting.

ATR-SEIRAS observations on the $\text{Pd}_3\text{Ni}_1\text{-TaN/C}$ and Pd-TaN/C catalysts during the alkaline MOR indicates that their anti-CO poisoning abilities are significantly enhanced, consistent with the CO-stripping tests. DFT calculations also further confirm that the OH adsorption is significantly enhanced as well as the CO adsorption is significantly reduced on the $\text{Pd}_3\text{Ni}_1\text{-TaN/C}$ and Pd-TaN/C catalysts, resulting in the elevated tolerance to CO.

In order to better uncover the guiding significance of the d-band electronic structures on the catalytic performance, two relationships, the onset potential of CO stripping VS the d-band centers, and the MOR activity VS the d-band centers, are plotted in Fig. 10(c-d). Interestingly, two approximate linear relationships are obtained. The result reveals that the rational d-band center can bring the lower CO adsorption energies on the catalyst surface, which will further affect the catalytic performance for MOR. It has been reported that the negatively-shifted d-band center may reduce the donation to the anti-bonding $\text{CO } 2\pi^*$ orbitals, which makes it facile to oxidize CO and further improves the anti-poisoning ability [32,99,100]. Therefore, Ni-induced surface defects-rich $\text{Pd}_3\text{Ni}_1\text{-TaN/C}$ catalyst exhibits the optimal d-band center and the appropriate adsorption of the intermediates, making it an efficient electrocatalyst towards MOR in alkaline medium with high anti-CO poisoning ability, good catalytic activity and stability.

For another, more importantly, the unique structure brings the variation of the reaction pathways. The in situ ATR-SEIRAS results demonstrate that, at the molecular level, compared to the CO-pathway on commercial Pd/C catalyst, MOR in alkaline media favors the non-CO pathway (that is, HCOO_{ad} pathway) on both the $\text{Pd}_3\text{Ni}_1\text{-TaN/C}$ and Pd-TaN/C catalysts. That is, TaN modification is beneficial for the HCOO_{ad} pathway for the alkaline MOR on the Pd-based catalysts, which may be due to the structural advantages of core-shell like structure of TaN and the presence of nitrogen vacancies, as demonstrated by HAADF and EXAFS results. Furthermore, by comparing the $\text{Pd}_3\text{Ni}_1\text{-TaN/C}$ and Pd-TaN/C catalysts, it is found that Ni modification can accelerate the

HCOO_{ad} pathway for the alkaline MOR on the $\text{Pd}_3\text{Ni}_1\text{-TaN/C}$ catalyst, indicating that highly dispersed Ni oxide/hydroxide species in $\text{Pd}_3\text{Ni}_1\text{-TaN/C}$ are also beneficial to further boost MOR in alkaline medium, as demonstrated by HAADF, XPS, EXAFS, in situ ATR-SEIRAS and electrochemical results. Specifically, abundant $\text{Ni(OH)}_2/\text{NiOOH}$ in $\text{Pd}_3\text{Ni}_1\text{-TaN/C}$ also significantly activates H_2O molecules to generate dangling O-H on the surface, leading that $\text{Pd}_3\text{Ni}_1\text{-TaN/C}$ shows excellent activity and anti-CO poisoning ability towards the alkaline MOR. DFT calculations further confirms that lower energy barriers of the formation of COOH occur on the $\text{Pd}_4\text{-Ni(OH)}_2\text{-TaN(001)}$ and $\text{Pd}_4\text{-Ni(OH)}_2\text{-TaN(001)-V}$ surfaces, implying that the removal of adsorbed is much easier and the introduction of Ni species and nitrogen vacancies can enhance the catalytic performance for MOR.

Taken together, combined with the above structural characterization results, the unsaturated coordination environment of $\text{Pd}_3\text{Ni}_1\text{-TaN/C}$ and the core-shell like morphology with fruitful active sites enable the as-synthesized $\text{Pd}_3\text{Ni}_1\text{-TaN/C}$ promising as an efficient electrocatalyst for alkaline MOR.

4. Conclusion

In summary, $\text{Ni(OH)}_2/\text{NiOOH}$ decorated $\text{Pd}_3\text{Ni}_1\text{-TaN/C}$ catalyst has been synthesized by a mild and simple solvothermal method, which elevates the alkaline MOR performance ($3636.36 \text{ A g}_{\text{Pd}}^{-1}$) by over 17 folds that of commercial Pd/C catalyst. This can be attributed to its unique core-shell like structure that is rich in highly dispersed Ni sites and nitrogen vacancies, as revealed by HAADF, XPS and EXAFS characterizations, which contributes to the fruitful active sites and the down-shifted d-band center, thus remarkably elevating the MOR performance. Additionally, during the MOR process, in situ ATR-SEIRAS results demonstrate that, different from the only CO-pathway on commercial Pd/C catalyst, it is the modification of nitrogen vacancy-abundant TaN that alters the MOR reaction pathway, that is, MOR occurs via the only

HCOO_{ad} pathway on the TaN-modified Pd catalysts, which is followed by easy splitting of C-H bond to generate CO₂ subsequently. Besides, compared to Pd-TaN/C, the abundant Ni(OH)₂/NiOOH in Pd₃Ni₁-TaN/C also significantly activates H₂O molecules to generate dangling O-H on the surface, making Pd₃Ni₁-TaN/C exhibit high activity and anti-CO poisoning ability towards the alkaline MOR, as supported by the CV, CO stripping and in situ ATR-SEIRAS results. DFT calculations also indicate that the introduction of Ni species and nitrogen vacancies enhances the CO tolerance with reducing the CO binding energy and the energy barrier of COOH generation from adsorbed CO with OH species. This work suggests a new strategy for the design and synthesis of vacancy-deficient Pd_xNi_y-TaN/C with the enhanced MOR catalytic performance. Understanding the roles of transition metal nitrides and the oxyphilic metal may shed light on the rational design of efficient TaN-doped Pd-based catalysts for alkaline direct alcohol fuel cells.

CRedit authorship contribution statement

Ye Na: Conceptualization, Methodology, Software, Validation, Formal analysis, Investigation, Data curation, Writing – original draft preparation, Visualization. **Zhao Pengcheng:** Resources, Software, Data curation, Formal analysis, Writing – review & editing. **Qi Xiaoying:** Writing – review & editing. **Zhang Riguang:** Resources, Writing – review & editing, Supervision. **Yan Binhang:** Resources, Writing – review & editing, Supervision. **Sheng Wenchao:** Resources, Writing – review & editing, Supervision. **Jiang Zhao:** Conceptualization, Methodology, Software, Resources, Writing – review & editing, Supervision, Project administration, Funding acquisition. **Fang Tao:** Resources, Supervision, Project administration, Funding acquisition.

Declaration of Competing Interest

The authors declare that they have no known competing financial interests or personal relationships that could have appeared to influence the work reported in this paper.

Data Availability

Data will be made available on request.

Acknowledgements

The authors greatly appreciate the following financial supports: the National Natural Science Foundation of China (22075225, 21706203, 22038011 and 22005236), Special Guidance Funds for the Construction of World-Class Universities (Disciplines) and Characteristic Development in Central Universities (PY3A076), China Postdoctoral Science Foundation (2020T130508, 2019M660258 and 2019M663731), Natural Science Basic Research Plan in Shaanxi Province of China (2020JQ-023, 2022JZ-07), Fundamental Research Funds for the Central Universities (cxtd2017004, xjj2018035 and xjh012020030 in Xi'an Jiaotong University), State Key Laboratory of Clean and Efficient Coal Utilization, Taiyuan University of Technology (SKL202105), Shaanxi Creative Talents Promotion Plan-Technological Innovation Team (2019TD-039), research funding from Beilin District (GX2017). The authors would like to thank for the Instrument Analysis Center of Xi'an Jiaotong University, who provided guidance of characterization.

Appendix A. Supporting information

Supplementary data associated with this article can be found in the online version at [doi:10.1016/j.apcatb.2022.122142](https://doi.org/10.1016/j.apcatb.2022.122142).

References

- [1] L. Tao, Y. Wang, Y. Zou, N. Zhang, Y. Zhang, Y. Wu, Y. Wang, R. Chen, S. Wang, Charge transfer modulated activity of carbon-based electrocatalysts, *Adv. Energy Mater.* 10 (2019) 1901227.
- [2] Y. Duan, J.Y. Lee, S. Xi, Y. Sun, J. Ge, S.J.H. Ong, Y. Chen, S. Dou, F. Meng, C. Diao, A.C. Fisher, X. Wang, G.G. Scherer, A. Grimaud, Z.J. Xu, Anodic oxidation enabled cation leaching for promoting surface reconstruction in water oxidation, *Angew. Chem. Int. Ed.* 60 (2021) 7418–7425.
- [3] C. Xie, D. Yan, W. Chen, Y. Zou, R. Chen, S. Zang, Y. Wang, X. Yao, S. Wang, Insight into the design of defect electrocatalysts: from electronic structure to adsorption energy, *Mater. Today* 31 (2019) 47–68.
- [4] J. Li, Z. Zhou, H. Xu, C. Wang, S. Hata, Z. Dai, Y. Shiraishi, Y. Du, In situ nanopores enrichment of Mesh-like palladium nanoplates for bifunctional fuel cell reactions: a joint etching strategy, *J. Colloid Interface Sci.* 611 (2022) 523–532.
- [5] J. Li, C. Wang, H. Shang, Y. Wang, H. You, H. Xu, Y. Du, Metal-modified PtTe₂ nanorods: Surface reconstruction for efficient methanol oxidation electrocatalysis, *Chem. Eng. J.* 424 (2021), 130319.
- [6] K. Zhang, C. Wang, F. Gao, S. Guo, Y. Zhang, X. Wang, S. Hata, Y. Shiraishi, Y. Du, Recent progress in ultrafine 3D Pd-based nanocubes with multiple structures for advanced fuel cells electrocatalysis, *Coord. Chem. Rev.* 472 (2022), 214775.
- [7] B. Zhang, F. Yang, H. Liu, L. Yan, W. Yang, C. Xu, S. Huang, Q. Li, W. Bao, B. Liu, Y. Li, Assembling graphene-encapsulated Pd/TiO₂ nanosphere with hierarchical architecture for high-performance visible-light-assisted methanol electro-oxidation material, *Ind. Eng. Chem. Res.* 58 (2019) 19486–19494.
- [8] B. Zhang, F. Yang, X. Zhang, N. Wu, B. Liu, Y. Li, Construction of graphene-wrapped Pd/TiO₂ hollow spheres with enhanced anti-CO poisoning capability toward photoassisted methanol oxidation reaction, *ACS Sustain. Chem. Eng.* 9 (2021) 1352–1360.
- [9] S. Li, A. Guan, H. Wang, Y. Yan, H. Huang, C. Jing, L. Zhang, L. Zhang, G. Zheng, Hybrid palladium nanoparticles and nickel single atom catalysts for efficient electrocatalytic ethanol oxidation, *J. Mater. Chem. A* 10 (2022) 6129–6133.
- [10] H. Peng, J. Ren, Y. Wang, Y. Xiong, Q. Wang, Q. Li, X. Zhao, L. Zhan, L. Zheng, Y. Tang, Y. Lei, One-stone, two birds: Alloying effect and surface defects induced by Pt on Cu₂-xSe nanowires to boost C-C bond cleavage for electrocatalytic ethanol oxidation, *Nano Energy* 88 (2021), 106307.
- [11] M. Qiao, Y. Wang, Q. Wang, G. Hu, X. Mamat, S. Zhang, S. Wang, Hierarchically ordered porous carbon with atomically dispersed FeN₄ for ultraefficient oxygen reduction reaction in proton-exchange membrane fuel cells, *Angew. Chem. Int. Ed.* 59 (2020) 2688–2694.
- [12] N. Ye, Y. Bai, Z. Jiang, T. Fang, Component-dependent activity of bimetallic PdCu and PdNi electrocatalysts for methanol oxidation reaction in alkaline media, *Int. J. Hydrog. Energy* 45 (2020) 32022–32038.
- [13] F. Wu, L. Zhang, J. Lai, R. Luque, W. Niu, G. Xu, Modulating the oxophilic properties of inorganic nanomaterials for electrocatalysis of small carbonaceous molecules, *Nano Today* 29 (2019), 100802.
- [14] N. Ye, P. Zhao, X. Qi, W. Sheng, Z. Jiang, T. Fang, Understanding the high performance of PdSn-TaN(tantalum nitride)/C electrocatalysts for the methanol oxidation reaction: coupling nitrides and oxophilic elements, *J. Mater. Chem. A* 10 (2021) 266–287.
- [15] Y. He, P. Ma, S. Zhu, M. Liu, Q. Dong, J. Espano, X. Yao, D. Wang, Photo-induced performance enhancement of tantalum nitride for solar water oxidation, *Joule* 1 (2017) 831–842.
- [16] L. Wang, B. Zhang, Q. Rui, Plasma-induced vacancy defects in oxygen evolution cocatalysts on Ta₃N₅ photoanodes promoting solar water splitting, *ACS Catal.* 8 (2018) 10564–10572.
- [17] M. Xiao, Z. Wang, B. Luo, S. Wang, L. Wang, Enhancing photocatalytic activity of tantalum nitride by rational suppression of bulk, interface and surface charge recombination, *Appl. Catal. B: Environ.* 246 (2019) 195–201.
- [18] Z. Lin, S.C. Ammal, S.R. Denny, S.A. Rytov, K. You, A. Heyden, J.G. Chen, Unraveling unique surface chemistry of transition metal nitrides in controlling selective C-O bond scission pathways of glycerol, *JACS* 2 (2022) 367–379.
- [19] F. Zhang, S. Xi, G. Lin, X. Hu, X.W.D. Lou, K. Xie, Metallic porous iron nitride and tantalum nitride single crystals with enhanced electrocatalysis performance, *Adv. Mater.* 31 (2019) 1806552.
- [20] N. Ye, Y. Bai, Z. Jiang, T. Fang, Design the PdCu/TaN C electrocatalyst with core-shell structure having high efficiency for methanol and formic acid oxidation reactions, *Electrochim. Acta* 383 (2021), 138365.
- [21] S. Goedecker, M. Teter, J. Hutter, Separable dual space gaussian pseudo-potentials, *Phys. Rev. B Condens Matter* 54 (1996) 1703–1710.
- [22] J.P. Perdew, K. Burke, M. Ernzerhof, Generalized gradient approximation made simple, *Phys. Rev. Lett.* 77 (1996) 3865–3868.
- [23] H.J. Monkhorst, J.D. Pack, Special points for Brillouin-zone integrations, *Phys. Rev. B* 13 (1976) 5188–5192.
- [24] M. Xiao, Z. Wang, B. Luo, S. Wang, L. Wang, Enhancing photocatalytic activity of tantalum nitride by rational suppression of bulk, interface and surface charge recombination, *Appl. Catal. B: Environ.* 246 (2019) 195–201.
- [25] Z. Jiang, Q. Zhang, Z. Liang, J.G. Chen, Pt-modified TaC as an efficient electrocatalyst for ethanol oxidation in acid and alkaline electrolytes, *Appl. Catal. B: Environ.* 234 (2018) 329–336.
- [26] M. Wassner, M. Eckardt, C. Gebauer, G.R. Bourret, N. Hüsing, R.J. Behm, Synthesis and electrocatalytic performance of spherical core-shell tantalum (oxy) nitride@nitrided carbon composites in the oxygen reduction reaction, *Electrochim. Acta* 227 (2017) 367–381.

- [27] S. Hu, F. Munoz, J. Noborikawa, J. Haan, L. Scudiero, S. Ha, Carbon supported Pd-based bimetallic and trimetallic catalyst for formic acid electrochemical oxidation, *Appl. Catal. B: Environ.* 180 (2016) 758–765.
- [28] L. Sun, B. Liao, X. Ren, Y. Li, P. Zhang, L. Deng, Y. Gao, Ternary PdNi-based nanocrystals supported on nitrogen-doped reduced graphene oxide as highly active electrocatalysts for the oxygen reduction reaction, *Electrochim. Acta* 235 (2017) 543–552.
- [29] Y. Yang, X. Sun, G. Han, X. Liu, X. Zhang, Y. Sun, M. Zhang, Z. Cao, Y. Sun, Enhanced electrocatalytic hydrogen oxidation on Ni/NiO/C derived from a nickel-based metal–organic framework, *Angew. Chem. Int. Ed.* 58 (2019) 10644–10649.
- [30] Y.P. Wu, J.W. Tian, S. Liu, B. Li, J. Zhao, L.F. Ma, D.S. Li, Y.Q. Lan, X. Bu, Bi-microporous metal-organic frameworks with cubane $[M_4(OH)_4]$ ($M = Ni, Co$) clusters and pore-space partition for electrocatalytic methanol oxidation reaction, *Angew. Chem. Int. Ed.* 58 (2019) 12185–12189.
- [31] A.A. Dubale, Y. Zheng, H. Wang, R. Hübner, Y. Li, J. Yang, J. Zhang, N.K. Sethi, L. He, Z. Zheng, W. Liu, High-performance bismuth-doped nickel aerogel electrocatalyst for the methanol oxidation reaction, *Angew. Chem. Int. Ed.* 59 (2020) 13891–13899.
- [32] R.S. Amin, R.M.A. Hameed, K.M. El Khatib, Microwave heated synthesis of carbon supported Pd, Ni and Pd-Ni nanoparticles for methanol oxidation in KOH solution, *Appl. Catal. B: Environ.* 148–149 (2014) 557–567.
- [33] J. Masud, M.T. Alam, Z. Awaludin, M.S. El-Deab, T. Okajima, T. Ohsaka, Electrocatalytic oxidation of methanol at tantalum oxide-modified Pt electrodes, *J. Power Sources* 220 (2012) 399–404.
- [34] Y. He, P. Ma, S. Zhu, M. Liu, Q. Dong, J. Espano, X. Yao, D. Wang, Photo-induced performance enhancement of tantalum nitride for solar water oxidation, *Joule* 1 (2017) 831–842.
- [35] C. Ho, K. Low, R.F. Klie, K. Maeda, K. Domen, R.J. Meyer, P.T. Snee, Synthesis and characterization of semiconductor tantalum nitride nanoparticles, *J. Phys. Chem. C* 115 (2011) 647–652.
- [36] L. Wang, B. Zhang, Q. Rui, Plasma-induced vacancy defects in oxygen evolution cocatalysts on Ta_3N_5 photoanodes promoting solar water splitting, *ACS Catal.* 8 (2018) 10564–10572.
- [37] Y. Zhou, S. Sun, S. Xi, Y. Duan, T. Sritharan, Y. Du, Z.J. Xu, Superexchange effects on oxygen reduction activity of edge-sharing $[Co_xMn_{1-x}O_6]$ octahedra in spinel oxide, *Adv. Mater.* 30 (2018) 1705407.
- [38] X. Ren, C. Wei, Y. Sun, X. Liu, F. Meng, X. Meng, S. Sun, S. Xi, Y. Du, Z. Bi, G. Shang, A.C. Fisher, L. Gu, Z.J. Xu, Constructing an adaptive heterojunction as a highly active catalyst for the oxygen evolution reaction, *Adv. Mater.* 32 (2020), e2001292.
- [39] C. Dai, Y. Sun, G. Chen, A.C. Fisher, Z.J. Xu, Electrochemical oxidation of nitrogen towards direct nitrate production on spinel oxides, *Angew. Chem. Int. Ed.* 59 (2020) 9418–9422.
- [40] H. Li, S. Sun, S. Xi, Y. Chen, T. Wang, Y. Du, M. Sherburne, J.W. Ager, A.C. Fisher, Z.J. Xu, Metal–oxygen hybridization determined activity in spinel-based oxygen evolution catalysts: a case study of $ZnFe_{2-x}Cr_xO_4$, *Chem. Mater.* 30 (2018) 6839–6848.
- [41] H. Li, Y. Chen, S. Xi, J. Wang, S. Sun, Y. Sun, Y. Du, Z.J. Xu, Degree of geometric tilting determines the activity of FeO_6 octahedra for water oxidation, *Chem. Mater.* 30 (2018) 4313–4320.
- [42] Y. Zhou, S. Sun, J. Song, S. Xi, B. Chen, Y. Du, A.C. Fisher, F. Cheng, X. Wang, H. Zhang, Z.J. Xu, Enlarged CoO covalency in octahedral sites leading to highly efficient spinel oxides for oxygen evolution reaction, *Adv. Mater.* 30 (2018) 1802912.
- [43] C. Wei, Z. Feng, G.G. Scherer, J. Barber, Y. Shao Horn, Z.J. Xu, A.I.U.S. Argonne, Cations in octahedral sites: a descriptor for oxygen electrocatalysis on transition-metal spinels, *Adv. Mater.* 29 (2017) 1606800.
- [44] C. Wei, Z. Feng, M. Baisariyev, L. Yu, L. Zeng, T. Wu, H. Zhao, Y. Huang, M. J. Bedzyk, T. Sritharan, Z.J. Xu, Valence change ability and geometrical occupation of substitution cations determine the pseudocapacitance of spinel ferrite $XFeyO_4$ ($X = Mn, Co, Ni, Fe$), *Chem. Mater.* 28 (2016) 4129–4133.
- [45] T. Wu, S. Sun, J. Song, S. Xi, Y. Du, B. Chen, W.A. Sasangka, H. Liao, C.L. Gan, G. G. Scherer, L. Zeng, H. Wang, H. Li, A. Grimaud, Z.J. Xu, Iron-facilitated dynamic active-site generation on spinel $CoAl_2O_4$ with self-termination of surface reconstruction for water oxidation, *Nat. Catal.* 2 (2019) 763–772.
- [46] T. Wang, J. Wang, Y. Sun, Y. Duan, S. Sun, X. Hu, S. Xi, Y. Du, C. Wang, Z.J. Xu, Origin of electronic structure dependent activity of spinel $ZnNi_{1-x}Co_{2x}O_4$ oxides for complete methane oxidation, *Appl. Catal. B: Environ.* 256 (2019), 117844.
- [47] X. Fu, W. Yu, C. Ma, J. Lin, S. Sun, S. Li, P. Ren, F. Jia, M. Li, W. Wang, X. Wang, C. Jia, K. Wu, R. Si, C. Yan, Supported Fe_2C catalysts originated from Fe_2N phase and active for Fischer-Tropsch synthesis, *Appl. Catal. B: Environ.* 284 (2021), 119702.
- [48] T. Wang, C. Zhang, J. Wang, H. Li, Y. Duan, Z. Liu, J.Y. Lee, X. Hu, S. Xi, Y. Du, S. Sun, X. Liu, J. Lee, C. Wang, Z.J. Xu, The interplay between the suprafacial and intrafacial mechanisms for complete methane oxidation on substituted $LaCoO_3$ perovskite oxides, *J. Catal.* 390 (2020) 1–11.
- [49] R.R. Chen, Y. Sun, S. Ong, S. Xi, Y. Du, C. Liu, O. Lev, Z.J. Xu, Antiferromagnetic inverse spinel oxide $LiCoVO_4$ with spin-polarized channels for water oxidation, *Adv. Mater.* 32 (2020), e1907976.
- [50] X. Jin, R. Wang, L. Zhang, R. Si, M. Shen, M. Wang, J. Tian, J. Shi, Electron configuration modulation of nickel single atoms for elevated photocatalytic hydrogen evolution, *Angew. Chem. Int. Ed.* 59 (2020) 6827–6831.
- [51] L. Jiang, J. Chen, R. Si, $LaO(OH)$ supported platinum catalysts for CO oxidation: deactivation by formation of lanthanum carbonate, *J. Rare Earth* 39 (2021) 297–304.
- [52] B. Nan, X. Hu, X. Wang, C. Jia, C. Ma, M. Li, R. Si, Effects of multiple platinum species on catalytic reactivity distinguished by electron microscopy and X-ray absorption spectroscopy techniques, *J. Phys. Chem. C* 121 (2017) 25805–25817.
- [53] P. Du, X. Hu, X. Wang, C. Ma, M. Du, J. Zeng, C. Jia, Y. Huang, R. Si, Synthesis and metal-support interaction of subnanometer copper-palladium bimetallic oxide clusters for catalytic oxidation of carbon monoxide, *Inorg. Chem. Front.* 4 (2017) 668–674.
- [54] C. Peng, Z. Xu, G. Luo, S. Yan, J. Zhang, S. Li, Y. Chen, L.Y. Chang, Z. Wang, T. K. Sham, G. Zheng, Highly-exposed single-interlayered Cu edges enable high-rate CO_2 -to- CH_4 electrosynthesis, *Adv. Energy Mater.* 12 (2022) 2200195.
- [55] Y. Chen, Y. Sun, M. Wang, J. Wang, H. Li, S. Xi, C. Wei, P. Xi, G.E. Sterbinsky, J. W. Freeland, A.C. Fisher, R.J.W. Ager, Z. Feng, Z.J. Xu, Lattice site-dependent metal leaching in perovskites toward a honeycomb-like water oxidation catalyst, *Sci. Adv.* 7 (2021) k1788.
- [56] Y. Chen, H. Li, J. Wang, Y. Du, S. Xi, Y. Sun, M. Sherburne, J.W. Ager, A.C. Fisher, Z.J. Xu, Exceptionally active iridium evolved from a pseudo-cubic perovskite for oxygen evolution in acid, *Nat. Commun.* 10 (2019).
- [57] P. Du, W. Wang, C. Jia, Q. Song, Y. Huang, R. Si, Effect of strongly bound copper species in copper-ceria catalyst for preferential oxidation of carbon monoxide, *Appl. Catal. A: Gen.* 518 (2016) 87–101.
- [58] B. Nan, Q. Fu, J. Yu, M. Shu, L. Zhou, J. Li, W. Wang, C. Jia, C. Ma, J. Chen, L. Li, R. Si, Unique structure of active platinum-bismuth site for oxidation of carbon monoxide, *Nat. Commun.* 12 (2021).
- [59] Y. Wang, J.L. Li, W.X. Shi, Z.M. Zhang, S. Guo, R. Si, M. Liu, H.C. Zhou, S. Yao, C. H. An, T.B. Lu, Unveiling single atom nucleation for isolating ultrafine fcc Ru nanoclusters with outstanding dehydrogenation activity, *Adv. Energy Mater.* 10 (2020) 2002138.
- [60] Y. Gu, X. Fu, P. Du, D. Gu, Z. Jin, Y. Huang, R. Si, L. Zheng, Q. Song, C. Jia, C. Weidenthaler, In situ X-ray diffraction study of Co-Al nanocomposites as catalysts for ammonia decomposition, *J. Phys. Chem. C* 119 (2015) 17102–17110.
- [61] L. Lin, Q. Yu, M. Peng, A. Li, S. Yao, S. Tian, X. Liu, A. Li, Z. Jiang, R. Gao, X. Han, Y. Li, X. Wen, W. Zhou, D. Ma, Atomically dispersed Ni/ α - MoC catalyst for hydrogen production from methanol/water, *J. Am. Chem. Soc.* 143 (2021) 309–317.
- [62] D. Chen, M. Qiao, Y.R. Lu, L. Hao, D. Liu, C.L. Dong, Y. Li, S. Wang, Preferential cation vacancies in perovskite hydroxide for the oxygen evolution reaction, *Angew. Chem. Int. Ed.* 57 (2018) 8691–8696.
- [63] Y. Zhao, X. Jia, G. Chen, L. Shang, G.I.N. Waterhouse, L. Wu, C. Tung, D.O. Hare, T. Zhang, Ultrafine NiO nanosheets stabilized by TiO_2 from monolayer NiTi-LDH precursors: an active water oxidation electrocatalyst, *J. Am. Chem. Soc.* 138 (2016) 6517–6524.
- [64] Y. Ji, Z. Chen, R. Wei, C. Yang, Y. Wang, J. Xu, H. Zhang, A. Guan, J. Chen, T. Sham, J. Luo, Y. Yang, X. Xu, G. Zheng, Selective CO-to-acetate electroreduction via intermediate adsorption tuning on ordered Cu–Pd sites, *Nat. Catal.* 5 (2022) 251–258.
- [65] L. Shang, X. Lv, L. Zhong, S. Li, G. Zheng, Efficient CO_2 electroreduction to ethanol by Cu_3Sn catalyst, *Small Methods* 6 (2022) 2101334.
- [66] Z. Huang, J. Song, Y. Du, S. Xi, S. Dou, J.M.V. Nsanzimana, C. Wang, Z.J. Xu, X. Zhang, Chemical and structural origin of lattice oxygen oxidation in Co–Zn oxyhydroxide oxygen evolution electrocatalysts, *Nat. Energy* 4 (2019) 329–338.
- [67] Y. Sun, X. Ren, S. Sun, Z. Liu, S. Xi, Z.J. Xu, Engineering high-spin state cobalt cations in spinel zinc cobalt oxide for spin channel propagation and active site enhancement in water oxidation, *Angew. Chem. Int. Ed.* 60 (2021) 14536–14544.
- [68] Z. Huang, S. Xi, J. Song, S. Dou, X. Li, Y. Du, C. Diao, Z.J. Xu, X. Wang, Tuning of lattice oxygen reactivity and scaling relation to construct better oxygen evolution electrocatalyst, *Nat. Commun.* 12 (2021).
- [69] C. Peng, X. Zhu, Z. Xu, S. Yan, L.Y. Chang, Z. Wang, J. Zhang, M. Chen, T.K. Sham, Y. Li, G. Zheng, Lithium vacancy-tuned $[CuO_4]$ sites for selective CO_2 electroreduction to C_2+ products, *SMALL* 18 (2022) 2106433.
- [70] C. Peng, G. Luo, Z. Xu, S. Yan, J. Zhang, M. Chen, L. Qian, W. Wei, Q. Han, G. Zheng, Lithiation-enabled high-density nitrogen vacancies electrocatalyze CO_2 to C_2 products, *Adv. Mater.* 33 (2021) 2103150.
- [71] C. Peng, G. Luo, J. Zhang, M. Chen, Z. Wang, T. Sham, L. Zhang, Y. Li, G. Zheng, Double sulfur vacancies by lithium tuning enhance CO_2 electroreduction to n-propanol, *Nat. Commun.* 12 (2021).
- [72] Q. Tan, C. Shu, J. Abbott, Q. Zhao, L. Liu, T. Qu, Y. Chen, H. Zhu, Y. Liu, G. Wu, Highly dispersed Pd- CoO_2 nanoparticles supported on N-doped core-shell structured mesoporous carbon for methanol oxidation in alkaline media, *ACS Catal.* 9 (2019) 6362–6371.
- [73] G. Orozco, M.C. Pérez, A. Rincón, C. Gutiérrez, Electrooxidation of methanol on silver in alkaline medium, *J. Electroanal. Chem.* 495 (2000) 71–78.
- [74] Y. Yang, J. Ren, H. Zhang, Z. Zhou, S. Sun, W. Cai, Infrared spectroelectrochemical study of dissociation and oxidation of methanol at a palladium electrode in alkaline solution, *Langmuir* 29 (2013) 1709–1716.
- [75] M. Li, D.A. Cullen, K. Sasaki, N.S. Marinkovic, K. More, R.R. Adzic, Ternary electrocatalysts for oxidizing ethanol to carbon dioxide: making Ir capable of splitting C–C bond, *J. Am. Chem. Soc.* 135 (2012) 132–141.
- [76] M.C. Figueiredo, R.M. Arán-Ais, J.M. Feliu, K. Kontturi, T. Kallio, Pt catalysts modified with Bi: enhancement of the catalytic activity for alcohol oxidation in alkaline media, *J. Catal.* 312 (2014) 78–86.
- [77] Q. Nian, J. Wang, S. Liu, T. Sun, S. Zheng, Y. Zhang, Z. Tao, J. Chen, Aqueous batteries operated at $-50^\circ C$, *Angew. Chem. Int. Ed.* 58 (2019) 16994–16999.
- [78] J.L. Bott-Neto, T.S. Martins, S.A.S. Machado, E.A. Ticianelli, Electrocatalytic oxidation of methanol, ethanol, and glycerol on $Ni(OH)_2$ nanoparticles

- encapsulated with poly[Ni(salen)] film, *ACS Appl. Mater. Interfaces* 11 (2019) 30810–30818.
- [79] Z. Zhou, N. Tian, Y. Chen, S. Chen, S. Sun, In situ rapid-scan time-resolved microscope FTIR spectroelectrochemistry: study of the dynamic processes of methanol oxidation on a nanostructured Pt electrode, *J. Electroanal. Chem.* 573 (2004) 111–119.
- [80] C. Qing-Song, S. Shi-Gang, Z. Zhi-You, C. Yan-Xin, D. Shi-Bin, CoPt nanoparticles and their catalytic properties in electrooxidation of CO and CH(3)OH studied by in situ FTIRS, *Phys. Chem. Chem. Phys.* 10 (2008).
- [81] T. Haisch, F. Kubannek, S. Baranton, C. Coutanceau, U. Krewer, The influence of adsorbed substances on alkaline methanol electro-oxidation, *Electrochim. Acta* 295 (2019) 278–285.
- [82] P.A. Christensen, A. Hamnett, D. Linares-Moya, The electro-oxidation of formate ions at a polycrystalline Pt electrode in alkaline solution: an in situ FTIR study, *Phys. Chem. Chem. Phys.* 13 (2011) 11739–11747.
- [83] F. Zhao, C. Li, Q. Yuan, F. Yang, B. Luo, Z. Xie, X. Yang, Z. Zhou, X. Wang, Trimetallic palladium-copper-cobalt alloy wavy nanowires improve ethanol electrooxidation in alkaline medium, *Nanoscale* 11 (2019) 19448–19454.
- [84] Y. Zhou, Y. Chen, K. Jiang, Z. Liu, Z. Mao, W. Zhang, W. Lin, W. Cai, Probing the enhanced methanol electrooxidation mechanism on platinum-metal oxide catalyst, *Appl. Catal. B: Environ.* 280 (2021), 119393.
- [85] Y.X. Chen, A. Miki, S. Ye, H. Sakai, M. Osawa, Formate, an active intermediate for direct oxidation of methanol on Pt electrode, *J. Am. Chem. Soc.* 125 (2003) 3680–3681.
- [86] X. Qin, H. Li, S. Xie, K. Li, T. Jiang, X. Ma, K. Jiang, Q. Zhang, O. Terasaki, Z. Wu, W. Cai, Mechanistic analysis-guided pd-based catalysts for efficient hydrogen production from formic acid dehydrogenation, *ACS Catal.* 10 (2020) 3921–3932.
- [87] J. Zhang, X. Qu, Y. Han, L. Shen, S. Yin, G. Li, Y. Jiang, S. Sun, Engineering PtRu bimetallic nanoparticles with adjustable alloying degree for methanol electrooxidation: Enhanced catalytic performance, *Appl. Catal. B: Environ.* 263 (2020), 118345.
- [88] F. Zhu, K. Tu, L. Huang, X. Qu, J. Zhang, H. Liao, Z. Zhou, Y. Jiang, S. Sun, High selectivity PtRh/RGO catalysts for ethanol electro-oxidation at low potentials: enhancing the efficiency of CO₂ from alcoholic groups, *Electrochim. Acta* 292 (2018) 208–216.
- [89] N. Ye, P. Zhao, X. Qi, W. Sheng, Z. Jiang, T. Fang, Ethanol electro-oxidation on the PdSn-TaN/C catalyst in alkaline media: Making TaN capable of splitting C C bond, *Appl. Catal. B: Environ.* 314 (2022), 121473.
- [90] Q. Zhang, Y. Ma, Y. Lu, L. Li, F. Wan, K. Zhang, J. Chen, Modulating electrolyte structure for ultralow temperature aqueous zinc batteries, *Nat. Commun.* 11 (2020).
- [91] L.F. Shen, B.A. Lu, Y.Y. Li, J. Liu, Z.C. Huang, H. Peng, J.Y. Ye, X.M. Qu, J. M. Zhang, G. Li, W.B. Cai, Y.X. Jiang, S.G. Sun, Interfacial structure of water as a new descriptor of the hydrogen evolution reaction, *Angew. Chem. Int. Ed.* 59 (2020) 22397–22402.
- [92] C. Li, J. Le, Y. Wang, S. Chen, Z. Yang, J. Li, J. Cheng, Z. Tian, In situ probing electrified interfacial water structures at atomically flat surfaces, *Nat. Mater.* 18 (2019) 697–701.
- [93] M. Arenz, K.J.J. Mayrhofer, V. Stamenkovic, B.B. Blizanac, T. Tomoyuki, P. N. Ross, N.M. Markovic, The effect of the particle size on the kinetics of CO electrooxidation on high surface area Pt catalysts, *J. Am. Chem. Soc.* 127 (2005) 6819–6829.
- [94] S. Lu, Z. Zhuang, Investigating the influences of the adsorbed species on catalytic activity for hydrogen oxidation reaction in alkaline electrolyte, *J. Am. Chem. Soc.* 139 (2017) 5156–5163.
- [95] T. Hofmann, T.H. Yu, M. Folse, L. Weinhardt, M. Bär, Y. Zhang, B.V. Merinov, D. J. Myers, W.A. Goddard, C. Heske, Using photoelectron spectroscopy and quantum mechanics to determine d-band energies of metals for catalytic applications, *J. Phys. Chem. C* 116 (2012) 24016–24026.
- [96] E. Toyoda, R. Jinnouchi, T. Hatanaka, Y. Morimoto, K. Mitsuhashi, A. Visikovskiy, Y. Kido, The d-band structure of Pt nanoclusters correlated with the catalytic activity for an oxygen reduction reaction, *J. Phys. Chem. C* 115 (2011) 21236–21240.
- [97] L. Bai, X. Wang, Q. Chen, Y. Ye, H. Zheng, J. Guo, Y. Yin, C. Gao, Explaining the size dependence in platinum-nanoparticle-catalyzed hydrogenation reactions, *Angew. Chem.* 128 (2016) 15885–15890.
- [98] X. Lu, M. Ahmadi, F.J. DiSalvo, H.D. Abruña, Enhancing the electrocatalytic activity of Pd/M (M = Ni, Mn) nanoparticles for the oxygen reduction reaction in alkaline media through electrochemical dealloying, *ACS Catal.* 10 (2020) 5891–5898.
- [99] H. Lei, X. Li, C. Sun, J. Zeng, S.S. Siwal, Q. Zhang, Galvanic replacement-mediated synthesis of Ni-supported Pd nanoparticles with strong metal-support interaction for methanol electro-oxidation, *Small* 15 (2019) 1804722.
- [100] H. Li, S. Zhao, M. Gong, C. Cui, D. He, H. Liang, L. Wu, S. Yu, Ultrathin PtPdTe nanowires as superior catalysts for methanol electrooxidation, *Angew. Chem. Int. Ed.* 52 (2013) 7472–7476.